PUBLISHED VERSION (DOI): 10.1016/j.ymssp.2019.04.043

A MULTIDISCIPLINARY APPROACH TO CALIBRATE ADVANCED NUMERICAL SIMULATIONS OF MASONRY ARCH BRIDGES

Álvaro Bautista-De Castro[1], Luis Javier Sánchez-Aparicio[1]*, Pedro Carrasco-García[1], Luís F. Ramos[2], Diego González-Aguilera[1]

[1]*Department of Cartographic and Land Engineering. University of Salamanca, High Polytechnic School of Ávila, Hornos Caleros, 50, 05003, Ávila (Spain)*

Tlf: +34 920353500; Fax: +34 920353501; alvarobautistadecastro@usal.es, luisj@usal.es, Retep81@usal.es, daguilera@usal.es,

[2]*ISISE, Department of Civil Engineering, University of Minho, Campus de Azurém, 4800-058 Guimarães, Portugal; lramos@civil.uminho.pt*

***Corresponding author: Tlf.: +34 920353500; Fax: +34 920353501**

E-mail address: luisj@usal.es

Abstract

The present paper proposes a robust multidisciplinary method, combining geomatic procedures (terrestrial laser scanning and reverse engineering), geophysic methods (ground penetrating radar and multichannel analysis of surface waves), sonic and impact echo tests and, ambient vibration approaches in order to generate accurate numerical simulations of masonry arch bridges. These methods are complemented by a robust finite element model updating method based on a metamodelling global sensitivity analysis and a robust calibration strategy. Results obtained corroborate the feasibility of the proposed methodology, with an average relative error in frequencies of 1.21% and an average modal assurance criterion of 0.93.

Keywords: masonry arch bridges; geomatic techniques; geophysic techniques; ambient vibration tests; sonic testing; finite element model updating.

1. Introduction

Throughout history, masonry arch bridges have been one of the most used constructions in the transportation networks, allowing the overpass of topographic accidents (such as gullies or rivers) and making possible the communication and trade between different places. Many of these masonry arch bridges, which was erected during the Roman and Mediaeval periods are still in use, supporting new traffic demands for which accurate numerical simulations are necesary [1].

Concerning this topic, the accurate structural evaluation of a masonry arch bridge requires an extensive knowledge of the different materials and structural systems presented on it. Within this context, several authors propose the use of multidisciplinary approaches, with the aim of characterizing the bridge at different levels [1-3]: (i) geometrical level; (ii) structural level and (iii) material level.

Regarding the geometry, some of these ancient constructions present complex and irregular shapes, characterized by the sucession of vaults and piers for which the photogrammetry as well as the terrestrial laser scanning has been placed as the most suitable solution [1, 2, 4]. The product of these procedures, the so-called point cloud, is later used to extract sections or individual measruements for the creation of the CAD models not exploiting the advantages offered by the last advances in reverse engineering [5]. These procedures are able to mimic non-parametric shapes (e.g. existing deformations) by means of b-splines methods and non-unirform b-spline approaches. Moreover, this type of bridges present a complex inner composition, where the ground penetrating radar has been considered as the most proper solution to characterize it, thus allowing to estimate the thicknesses of its spandrel walls, barrel vaults and the layering of infill materials

Concerning the material characterization, two are the main structural components of a masonry arch bridge: (i) the mansory and; (ii) the infill. On the one hand, the masonry is used for the construction of vaults, piers and sprandel walls and can be characterized in-situ through the use of sonic tests [1]. These tests allow the extraction of the Young Modulus and the Poisson’s coefficient through the analysis of the waves generated after the excitation of the material [6, 7]. On the other hand, the infill allows the stabilization of the vaults as well as appropiate transmission of loads coming from the pavements, being its mechanical and physiscal properties a critical issue in the structural stability of masonry arch bridges [1, 8-10]. Moreover, the accurate characterization of the mechanical and physical properties of infill materials results complex, being necessary the use of invasive techniques to extract samples, as well as another invasive methods (e.g. Ménard Pressuremeter tests) to locally obtain the infill parameters.

With respect to the structural characterization, many authors propose the use of the Ambient Vibration Tests as the most suitable strategy for the evaluation of the global behaviour of historical structures [5, 11, 12]. Being specially useful if the numerical simulation of the bridge is carried out by means of the finite element method, allowing the use of updating methods that enhance the accuracy of the model [1, 5]. During these updating strategies, it is required the use of sensitivity approaches able to evaluate the influence of each variable in the dynamic response of the bridge. However, the large computational cost of each numerical simulation needed for the sensitivity analysis, leads to the use of a low number of simulations to evaluate the sensitivity of each input by means of sensitivity methods based on the Linear Spearman correlation matrix or basic sensitivity analysis [1, 13]. Making it impossible the use of advanced and robust sensitvity methods such as the Sobol´s indexes [14]. These indexes require the use of the so-called Monte Carlo simulations in order to get reliable results for which it is needed the use of thousand of simulations [15].

Under the basis previously shown, this article proposes a new fully non-invasive multidisciplinary method able to overcome part of the main limitations detected in the structural evaluation of historical masonry arch bridges. To this end, the propose method will use the Terrestrial Laser Scanner, the Ground Penetrating Radar, the impact echo method and reverse engineering procedures to create as-built CAD models able the deformations presented on this type of structures. Moreover, the proposed approach also uses sonic tests for the mechanical characterization of the masonry elements; the multichannel analysis of surface waves method for the mechanical and physical characterization of the infill (without needding of using invasive techniques); Ambient Vibration Tests for the characterization of the global behaviour of the structure; and the finite element method for the advance numerical simulation of the bridge. Concerning the last one, the finite element model will be enhanced through the use of a robust updating method based on the Polynomial Chaos Expansion metamodelling strategy for the evaluation of the Sobol's indexes and the use of a non-linear least squares procedure to minimize the discrepancies between the numerical and the experimental data.

Particularly, this methodology has been applied in a real case study: the Arco masonry arch bridge, erected over the Alberche river and located in Avila region, Spain. This ancient construction seems to date back from the XVIth century according with the description detailed by [16] and later was modified at the beginning of the XXth century, in order to withstand the current traffic loads. Presenting this construction two different infills for which its is required the accurate mechanical and physical characterization.

The present paper is organized as follows: after this initial Introduction, Section 2 presents the Arco Bridge followed by Section 3 that shows the experimental campaign performed in this historical construction; Section 4 details the updating process of the numerical model; and finally, Section 5 presents the conclusions.

2. The Arco Bridge (Ávila, Spain)

2.1 Historical background

This historical masonry arch bridge is located in the road AV-901, connecting the municipalities of Burgohondo and Villanueva de Avila in the southeast region of Castile and León, Spain. Erected over the Alberche river, it is believed that its origin dates back from the 16th century according with its constructive characteristics [16]: (i) an eurhythmic design; (ii) the use of barrel vaults; (iii) the presence of a regular masonry and (iv) a road without variation of the width. Throughout its existence, this bridge has experimented modifications due to restauration works after its construction.

On 2 October 1920, the works for the construction of a road to connect Avila to the municipality of Casavieja were granted to the engineer D. Juan Manuel Torregrosa with a timeframe to finish them on 31 March 1923, being this bridge a part of this road. During the works, the original cambered road of the bridge was removed, adding a new layer of infill material, in addition to expand its spandrel walls and replacing its original parapets by others with larger width (Fig. 1a). However, due to the bad weather that it was presented in the place of the works in that epoch, the execution time was extended during eight months by the order of the Directorate General of Public Works, being finished them on 30 November 1923.

Of all provided information about restauration works in this historical construction, it is unknown when the wing wall (Fig. 1b) and the reinforced concrete on the pier (Fig. 1c) were added. However, according with the construction plans of the restoration works finished in 1923, it is known that both components were added after these rehabilitation works (Fig. 1a).

Finally, in the year 2010 the section of the road AV-901 from Burgohondo to Villanueva de Avila was widened with the exception of the bridge and the drainage was rehabilitated. As a result, only a layer of asphalt were added over the pavement of the bridge without to replace its parapets.

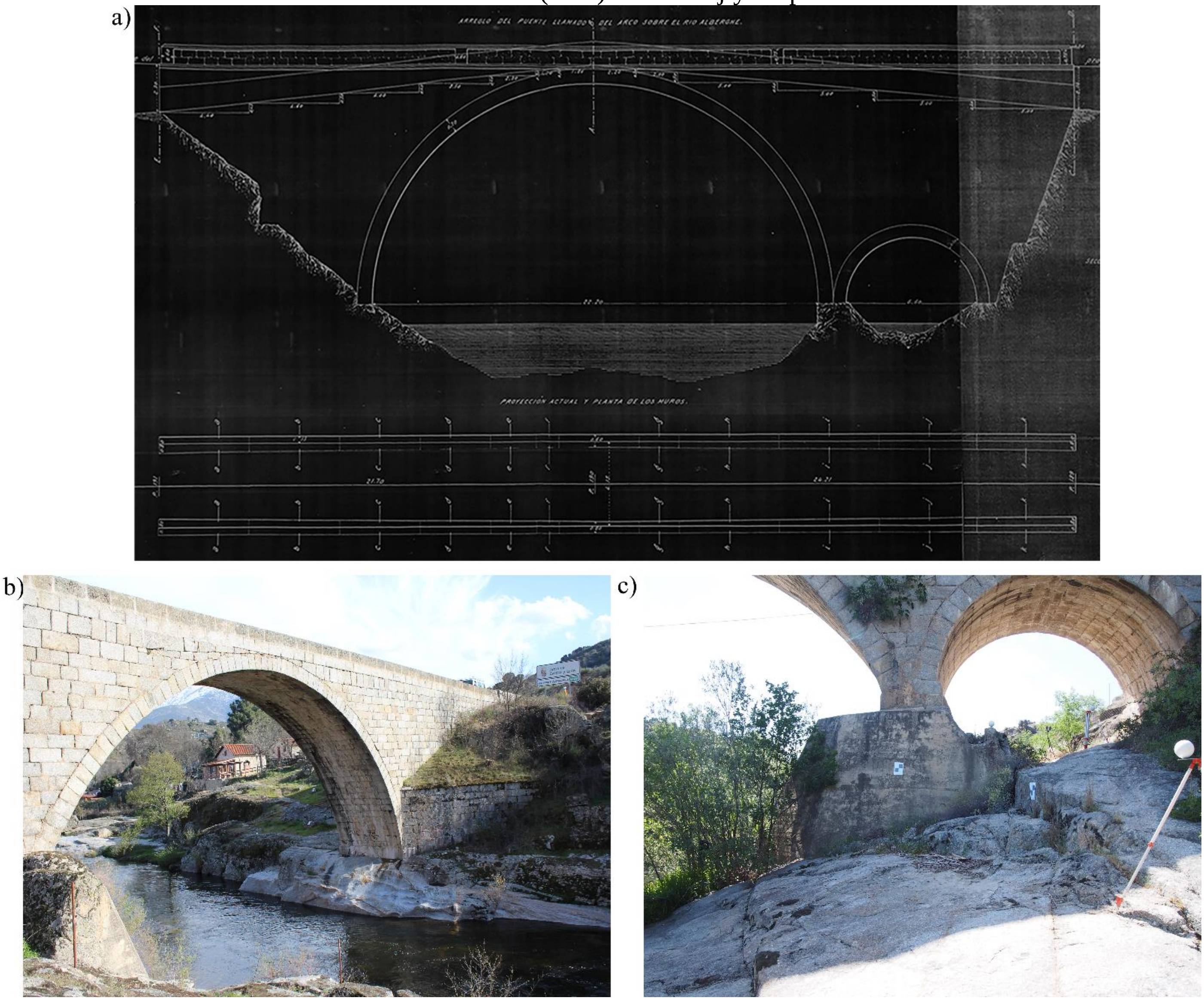

Figure 1: The Arco Bridge: a) downstream elevation before and after restoration works; b) upstream elevation and; c) reinforced concrete layer added to the pier between vaults.

2.2 Description of the ancient masonry arch bridge

This historical construction presents a total length of approximately 45.91 m. Furthermore, it shows the following structural components according with the existing drawings (Fig. 2): (i) a main barrel vault with a span of 22.20 m, a rise of 9.05 m and an average thickness of 0.70 m; (ii) a secondary barrel vault with a span of 6.60 m, a rise of 3.15 m and an average thickness of 0.60 m; (iii) spandrel walls with an average thickness of 0.60 m; (iv) a wing wall added after the rehabilitation works of 1923 and (v) a reinforced concrete pier between the two barrel vaults with a height of 4 m. Concerning its inner geometry, the bridge shows the following components: (i) a original infill layer with a maximum depht of 7.11 m and (ii) an added layer of infill material from the rehabilitation works of 1923 with maximum heights of 2.14 m and 2.30 m at the ends of the bridge.

Complementary to this, the non-structural elements of the bridge are (Fig. 2): (i) an asphalt pavement with 150 mm of thickness and (ii) two parapets with a height and width of 1000 mm and 400 mm, respectively.

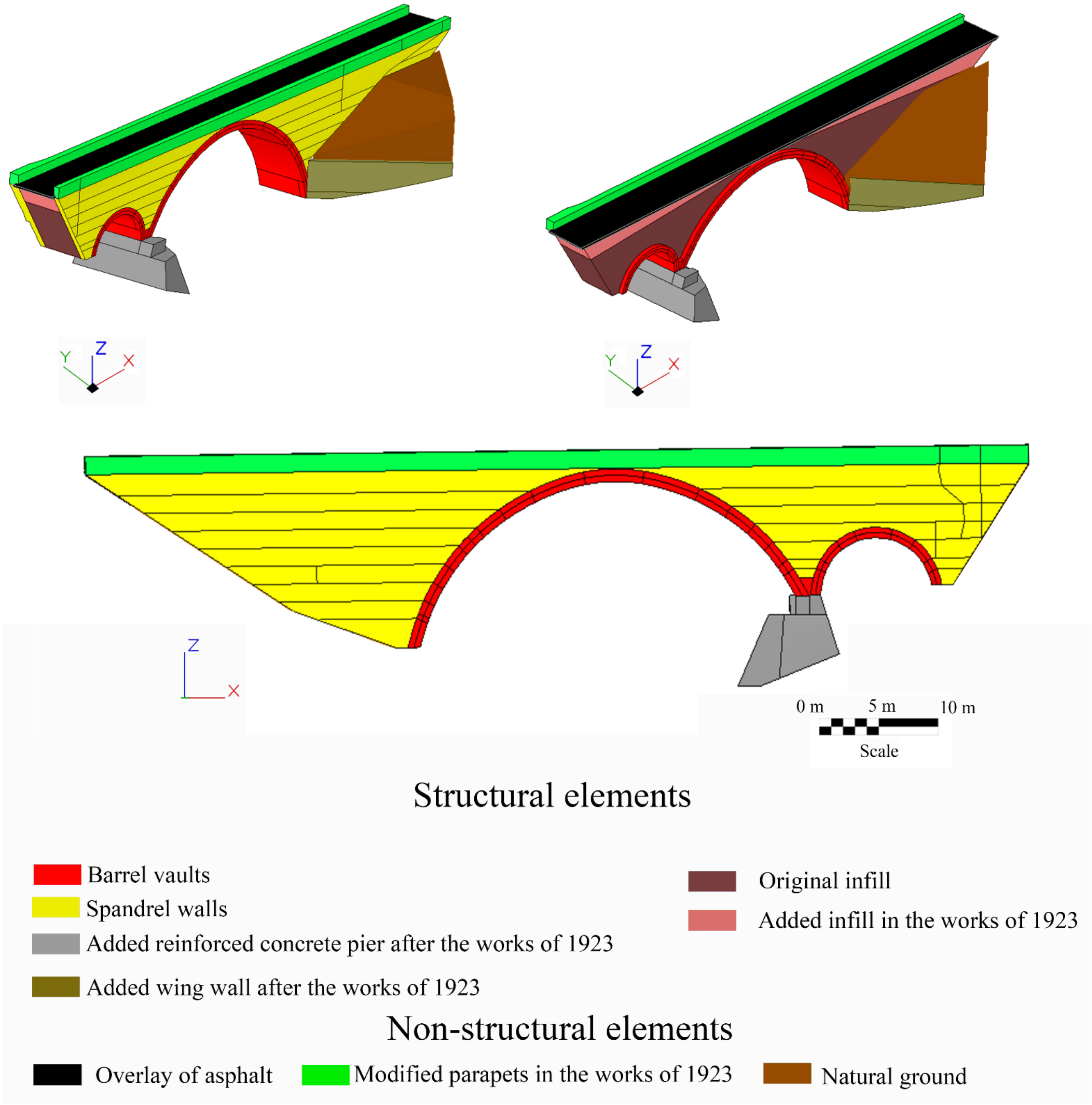

Figure 2: Structural elements and non-structural elements of the Arco Bridge.

2.3 Damage identification on the bridge: visual inspection

Prior to perform the experimental campaign on the bridge, a visual inspection was carried out in order to assess its current state, verifying the presence of different types of visual indicators of damage, namely (Fig. 3)(Fig. 4): (i) out of plane deformations and cracks in part of the spandrel walls; (ii) soiling and white crusts on the barrel vaults due to the salts of the mortar used to restore the barrel vaults; (iii) graffiti on the main barrel vault, on the wing wall and on a parapet; (iv) higher plants on the mortar joints of the spandrel walls and on the mortar joints between the barrel vaults and the spandrel walls; (v) lichens on the wing wall and (vi) moss. The origin of some of these damages, such as the out of plane deformations and cracks in its masonry, seem to be related with its current demands of traffic loads as well as of unexpected natural events produced in the past.

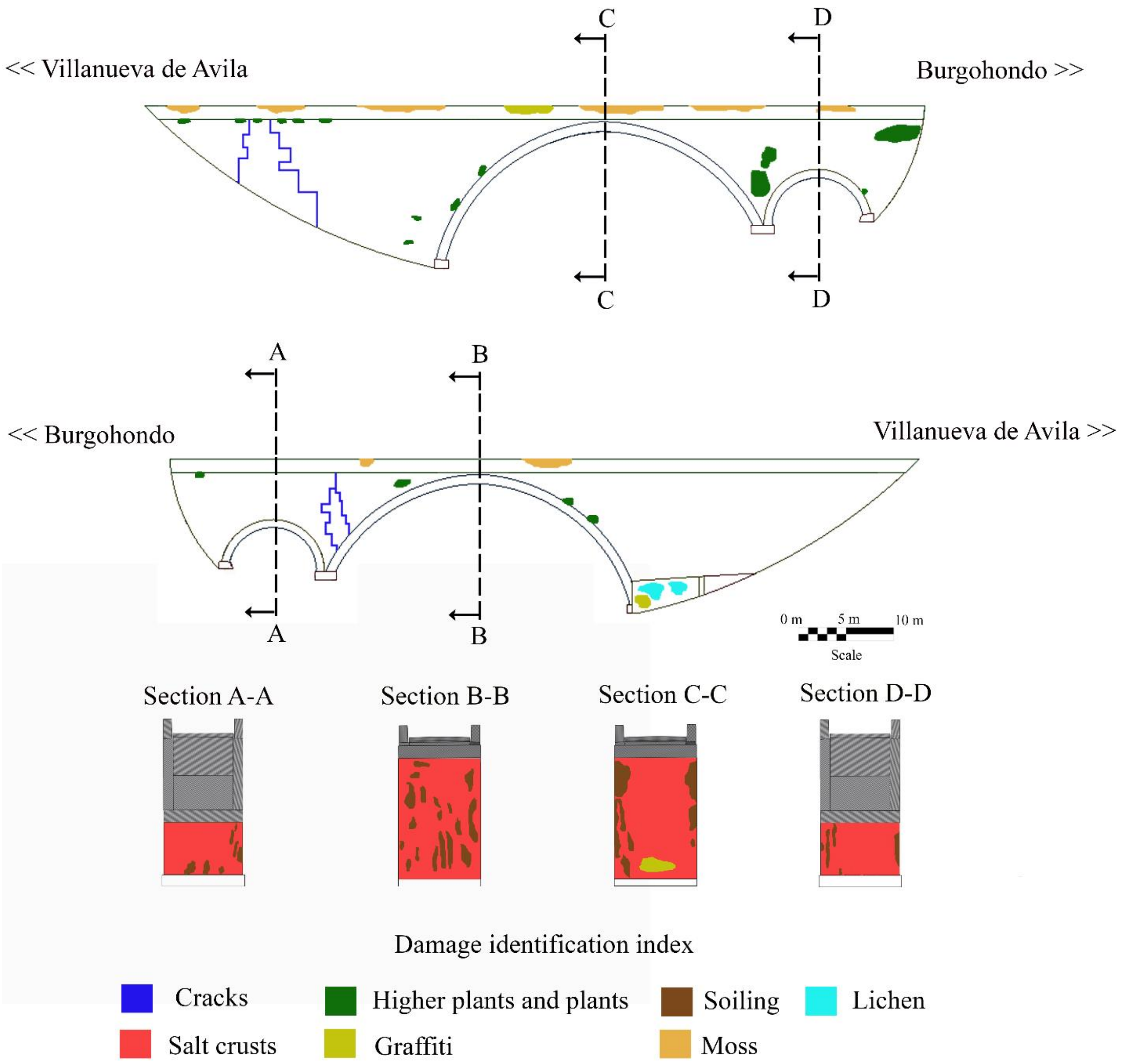

Figure 3: Damage mapping performed during the visual inspection.

Figure 4: Current state of conservation of the bridge: a) cracks on the spandrel wall; b) Salt crusts and soiling on the smaller barrel vault; c) Salt crusts, soiling, and graffiti on the bigger barrel vault and d) higher plants on the spandrel wall.

Additionally to the indicators of damage previously shown, it was possible to detect two type of masonries (Fig. 4): (i) a masonry with material losses in its joints in the sprandell walls and (ii) a masonry without material losses in its joints in the barrel vaults.

3. Experimental campaign: mechanical, geometrical and dynamical characterization of the Arco Bridge

Considering that for the accurate numerical simulation of the bridge it is required an extensive knowledge of the different structural components of the bridge, the following workflow was carried out (Fig. 5).

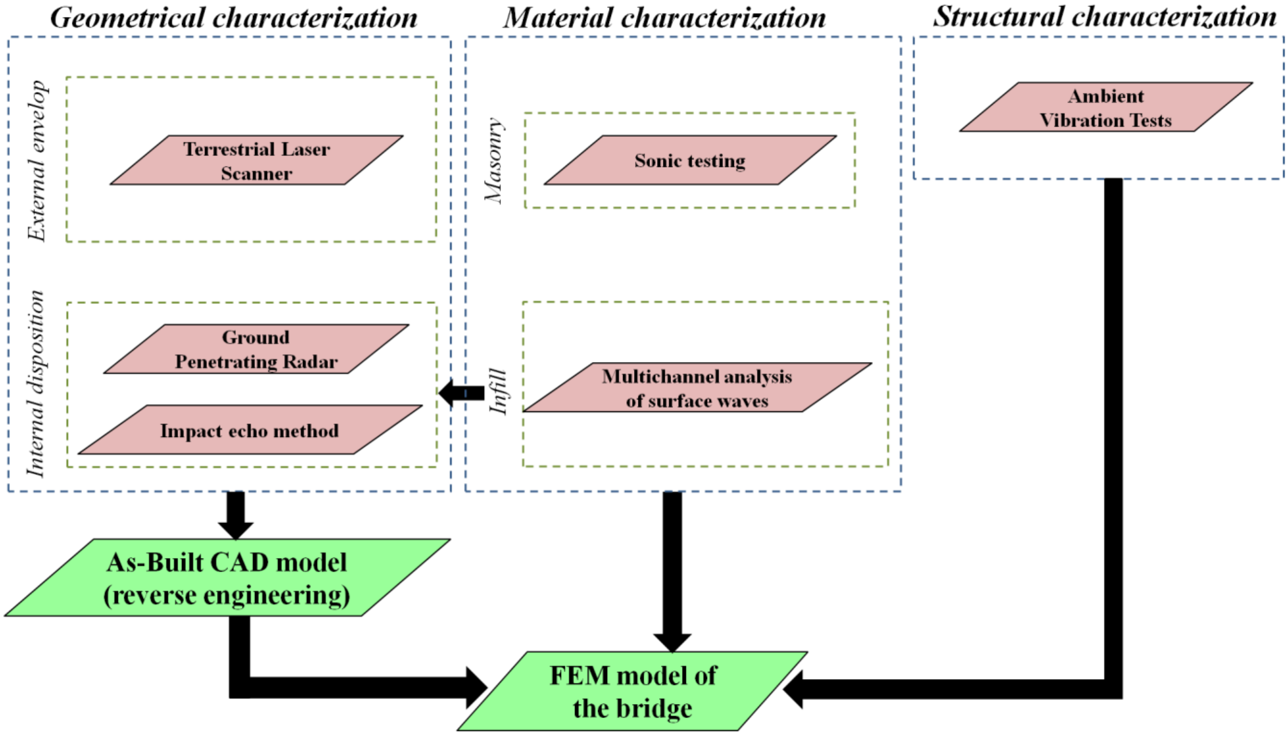

Figure 5: Workflow of the proposed methodology.

3.1 Mechanical characterization of materials: multichannel analysis of surface waves method and sonic tests

Built in masonry, the Arco Bridge is composed by grey granitic spandrel walls and grey granitic barrel vaults coming from the local quarries of Avila. Concerning its inner composition, the historical documentation (Section 2.1) revealed two layers of infill material (Fig. 2). According with this, and taking into account the relevance of an accurate characterization of the mechanical properties of these structural components, the following non-destructive techniques were used: (i) multichannel analysis of surface waves and (ii) sonic tests.

3.1.1 *Multichannel analysis of surface waves*

The infill of the bridge can be considered as a soil inserted winin the space delimited by its spandel walls and vaults. Considering this, Geophysics can offer a solution able to extract the mechanical and physical properties of the soils: the multichannel analysis of surface waves (MASW) [17, 18]. This method allows to extract the phase velocities and frequencies of the waves created after the excitation of a soil. This excitation was carried out by means of a 20.00 kg tenderizer connected to a data acquisition unit (Fig. 6) and captured through a linear array of 24 geophones with a natural frequency of 4.5 Hz. This sensors were placed along the bridge´s asphalted pavement, being separated between them a distance of 0.5 m in a total length of 11.5 m (Fig. 7). It is worth mentioning, and with the aim of evaluating the reliability of the data acquired that a total of 4 setups were carried out (Fig. 7).

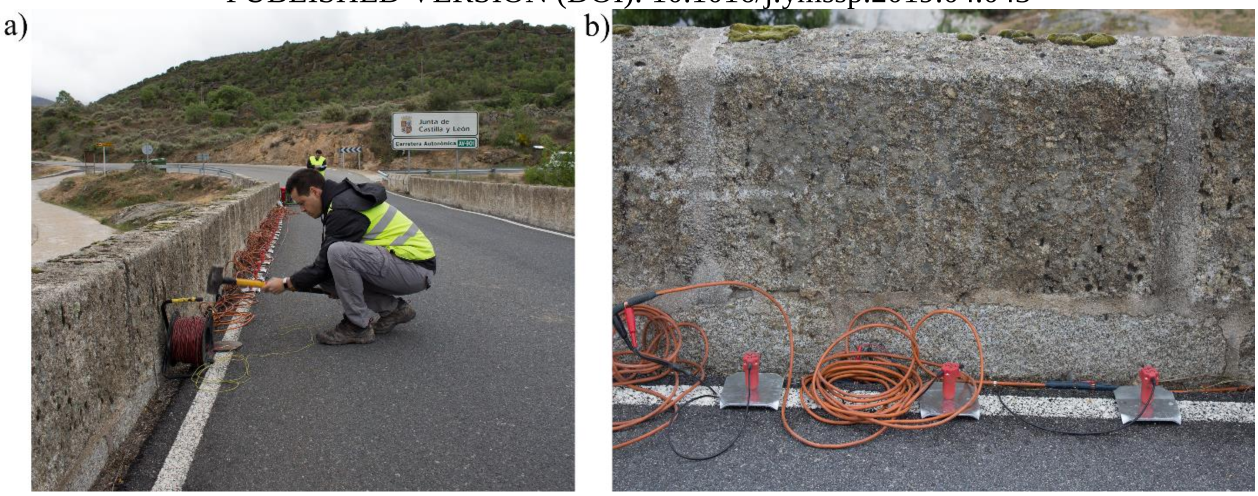

Figure 6: MASW test carried out on the bridge: a) instrumental hammer and b) geophones with a natural frequency of 4.5 Hz.

According with the constructive disposition of the bridge as well as the expected infill distribution (Fig. 2), four setups were carried out (Fig. 7). On each setup, a total of 24 geophones with a natural frequency of 4.5 Hz (Fig. 6b), were placed along the bridge´s asphalted pavement, being separated between them a distance of 0.5 m in a total length of 11.5 m (Fig. 7).

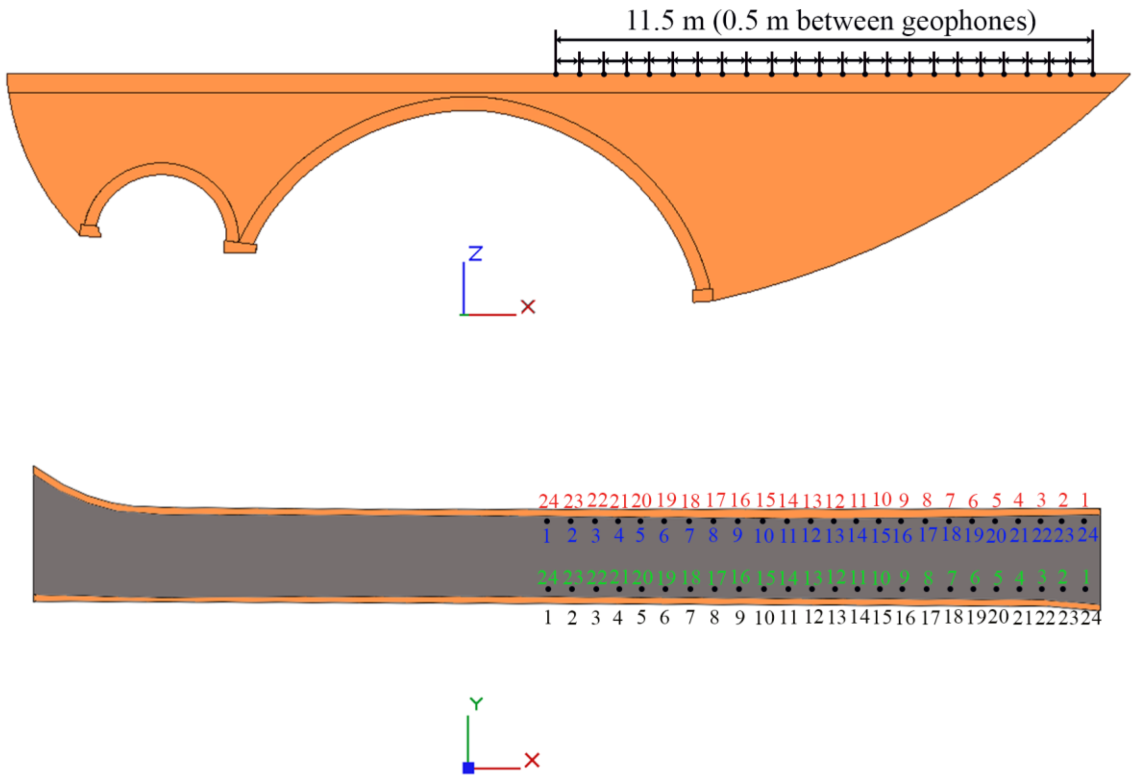

Position 1 of the 24 geophones

Setup 1: 1, 2, 3, 4, 5, 6, 7, 8, 9, 10, 11, 12, 13, 14, 15, 16, 17, 18, 19, 20, 21, 22, 23, 24

Setup 2: 1, 2, 3, 4, 5, 6, 7, 8, 9, 10, 11, 12, 13, 14, 15, 16, 17, 18, 19, 20, 21, 22, 23, 24

Position 2 of the 24 geophones

Setup 3: 1, 2, 3, 4, 5, 6, 7, 8, 9, 10, 11, 12, 13, 14, 15, 16, 17, 18, 19, 20, 21, 22, 23, 24

Setup 4: 1, 2, 3, 4, 5, 6, 7, 8, 9, 10, 11, 12, 13, 14, 15, 16, 17, 18, 19, 20, 21, 22, 23, 24

Figure 7: Setups and geophones positions used during the mechanical characterization of the two infill layers.

From the excitation captured by the geophones it was possible to extract the dispersion curve of the soil as well as its principal model. Then, a optimization procedure, also acalled inversion analysis, is performed in order to obtain the average shear-wave velocities of a soil (*Vs*) with respect to the depth (Fig. 8). Aditionally to this the method was able to record the primary-waves speeds (*Vp*). [17]. Then, these two speeds (*Vs* and *Vp*) are related with the Young's Modulus, the density, the Shear modulus and the Bulk modulus of the soil (Eq.1) (Eq.2) (Eq.3) (Eq.4).

$$\rho = 1.2475 + 0.399\left({}^{V_p}/_{1000}\right) - 0.026\left({}^{V_p}/_{1000}\right)^2 \tag{1}$$

$$E = \rho V_s^2 \frac{3\left(\frac{V_p}{V_s}\right)^2 - 4}{\left(\frac{V_p}{V_s}\right)^2 - 1} \tag{2}$$

$$G = \rho V_s^2 \tag{3}$$

$$K = \rho V_p^2 - \frac{4}{3} G \tag{4}$$

where ρ is the density in kg/m^3; E is the Young´s Modulus in GPa; V_p is the primary-wave speed of the soil in m/s; G is the Shear modulus in GPa; K is the Bulk modulus in GPa and; V_s is the shear-wave speed of the soil in m/s.

Additionally to these mechanical properties, the N_{spt} (number of blows from standard penetration tests) of a soil is obtained through Equation 5.

$$V_s = 85.35 N_{spt}^{0.348} \tag{5}$$

As a result, it has been possible to characterize the infills of the bridge from a mechanical and physical point of view (Table 1), as well as an estimation of its average dpeths by means of the V_s obtained during the experimental campaign (Fig. 8).

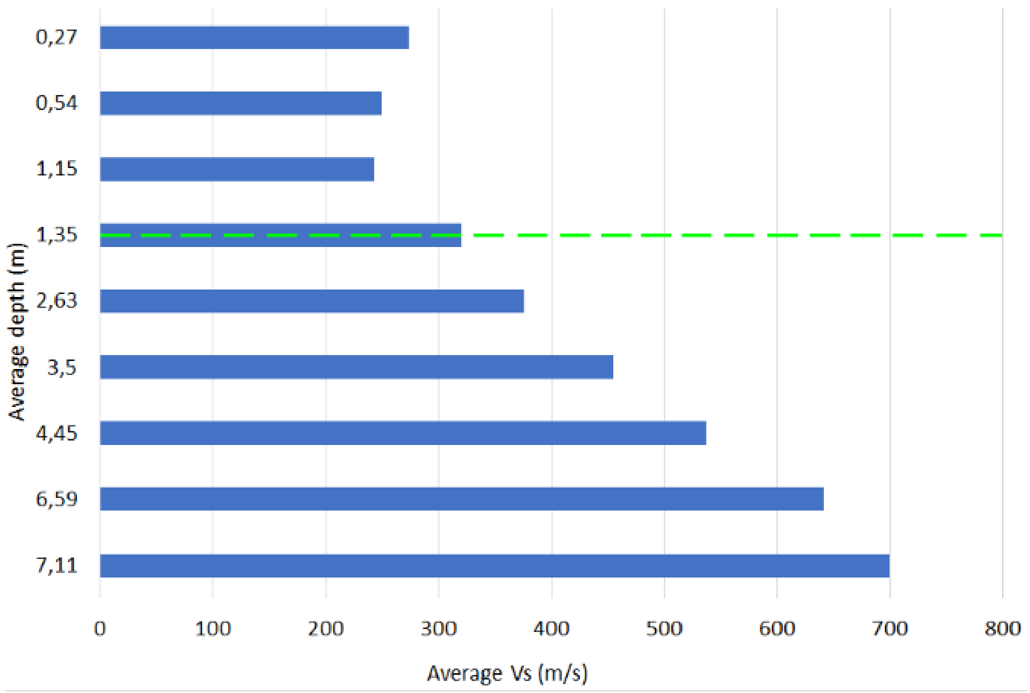

Figure 8: Estimation of the infill layers throught the relation between the average depths and the average V_s speeds. The green line represents the interface between the added and original infill layers.

Table 1: Upper bounds, lower bounds, average values and coefficients of variation (Cov) of the N-SPT, Young Modulus, shear modulus, bulk modulus, Poisson's ratio and density obtained from the MASW tests in the two infill materials. In brackets, the average depths of the added and original infill layers.

		Added infill layer (1.35 m)	Original infill layer (7.11 m)
N-SPT	Upper bound	57.29	581.97

	Lower bound	6.67	52.86
	Average value	29.37	283.54
	Cov (%)	51.02	59.96
Young Modulus (GPa)	Upper bound	0.78	3.18
	Lower bound	0.33	0.56
	Average value	0.41	1.73
	Cov (%)	24.46	41.25
Shear modulus (GPa)	Upper bound	0.19	0.96
	Lower bound	0.11	0.26
	Average value	0.14	0.60
	Cov (%)	34.54	42.08
Bulk modulus (GPa)	Upper bound	4.91	7.08
	Lower bound	3.90	4.88
	Average value	4.44	6.10
	Cov (%)	6.41	11.57
Poisson's ratio	Upper bound	0.50	0.46
	Lower bound	0.48	0.44
	Average value	0.49	0.45
	Cov (%)	0.90	1.18
Density (kg/m^3)	Upper bound	1847.00	1961.00
	Lower bound	1787.00	1848.00
	Average value	1819.00	1909.00
	Cov (%)	0.93	1.35

It is worth mentioning the large values obtained for the upper bounds of the "Original infill layer" (Table 1). This values can be explained by the presence of some intrusions of natural soil within the space delimited by the sprandell walls (Fig. 1) (Fig.2).

3.1.2 *Sonic testing*

Aditionally to the MASW tests, several indirect sonic tests were carried out in different places of the bridge with the aim of characterizing, from a mechanical point of view, the masonry (Fig. 8).

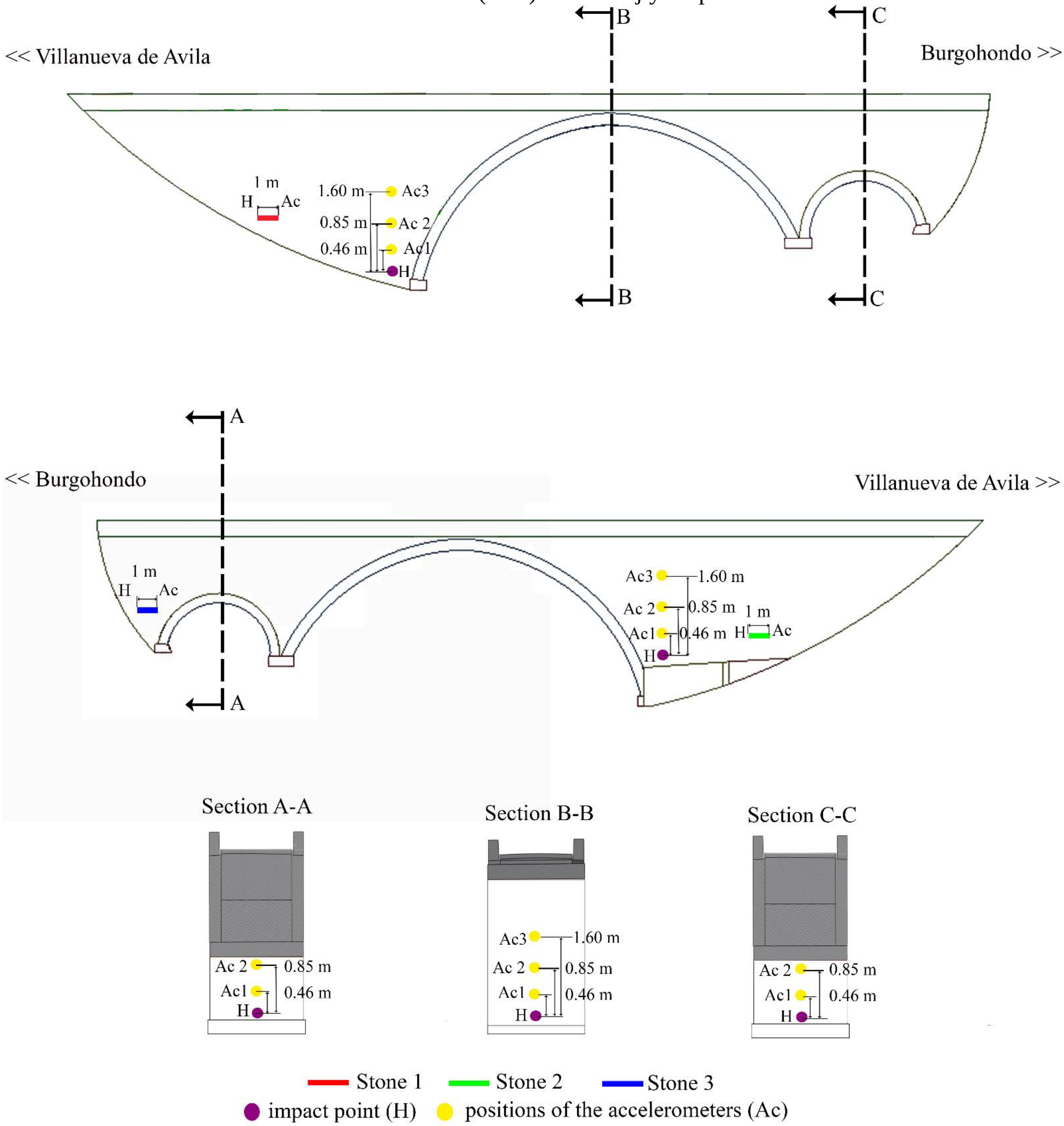

Figure 8: Places considered for the indirect sonic testing.

During these tests, an instrumental hammer, a data adquistion unit of 24 bit of resolution with a maximum sampling rate of 100 kHz and several piezoelectric accelerometers (transducers) with a sensitivity of 10 V/g, range of ±0.5g and 8μg rms broadband resolution were used. On each area evaluated, the material was excited with the instrumental hammer and its excitation, in form of compressional or primary waves (V_p) and surface or Rayleight waves (V_r), was recorded by the transducers. Then, the following equations were applied allowing the evaluation of the mechancial properties of the masonry (Eq. 1) (Eq. 2) (Eq. 3) [6] [19].

$$V_P = \left(\frac{\mathrm{E}\,(1-\nu)}{\rho(1-\nu)(1-2\nu)}\right)^{1/2} \tag{1}$$

$$V_r = \frac{0.87+1.12\nu}{1+\nu}\left(\frac{\mathrm{E}}{2\rho(1+\nu)}\right)^{1/2} \tag{2}$$

$$\frac{V_p}{V_r} = \frac{0.87+1.12\nu}{1+\nu}\left(\frac{(1-2\nu)}{2(1-\nu)}\right)^{1/2} \tag{3}$$

According with the results provided by the indirect sonic tests (Table 2), two different type of masonry can be considered: (i) the masonry of the sprandell walls which shown an average Young Modulus of 1.79 GPa and (ii) the masonry of the barrel vaults with an average Young Modulus of 3.28 GPa. These values are in agremment with the results obtained during the visual inspection (Section 2.3) and seem to be related with the conservation state of the joints, since the stones evaluated by means of indirect tests presented similar velocities (Fig. 8) (Table 3).

Table 2: Results obtained from the indirect sonic tests carried out on the bridge. It is worth mentioning, that a range of densities between 2000 and 2500 kg/m^3, were considered with the aim of obtaining a confidence range of admisible values for the different mechancial properties.

	Spandrel walls		Barrel vaults	
	P-wave	R-wave	P-wave	R-wave
Average velocity (m/s)	1110.00	588.00	1240.00	657.00
Cov (%)	1.56	1.75	0.68	0.55
Poisson´s coeffiecient	0.26		0.24	
Density (kg / m^3)	2000-2500		2000-2500	
Young´s modulus (GPa)	1.00-2.57		2.56-4.00	

Table 3: Results obtained from the indirect tests carried out on the stones.

	Stone 1		Stone 2		Stone 3	
	P-wave	R-wave	P-wave	R-wave	P-wave	R-wave
Average velocity (m/s)	1113.14	589.96	1146.56	607.68	1113.80	590.31
Cov (%)	0.10	0.08	1.12	1.08	0.06	0.04
Poisson´s coeffiecient	0.26		0.26		0.26	
Density (kg / m^3)	2000-2500		2000-2500		2000-2500	
Young´s modulus (GPa)	2.02-2.53		2.15-2.68		2.03-2.53	

3.2 External geometrical characterization: terrestrial laser scanning

Due to the difficulty to access in some parts of the bridge as well as the extension of the infrastructure, the use of a TLS is the best solution given its flexibility and quick data acquisition and processing. To this end, the lightweight TLS Faro Focus 3D 120® was used to digitalize the whole structure. This laser scanner is based on the phase shift physical principle [20], showing a great compromise between data acquisition rate and accuracy (Table 4).

Table 4: Technical specifications of the TLS Faro Focus 3D 120®.

Faro Focus 3D 120®	
Measurement principle	Phase shift
Wavelength	905 nm
Measurement range	0.6-120 m
Accuracy nominal value	2 mm to 25 m in normal conditions of illumination and reflectivity
Field of view	360º Horizontal 305º Vertical
Capture rate	122,000/976,000 points
Beam divergence	0.19 mrad

Added to the TLS system, several registration spheres with two different diameters (20 cm and 14.5 cm) and several planar targets (Fig. 9b), were used with the purpose to align automatically the different scan stations captured. To this end a target-based registration procedure was carried out.

a) b)

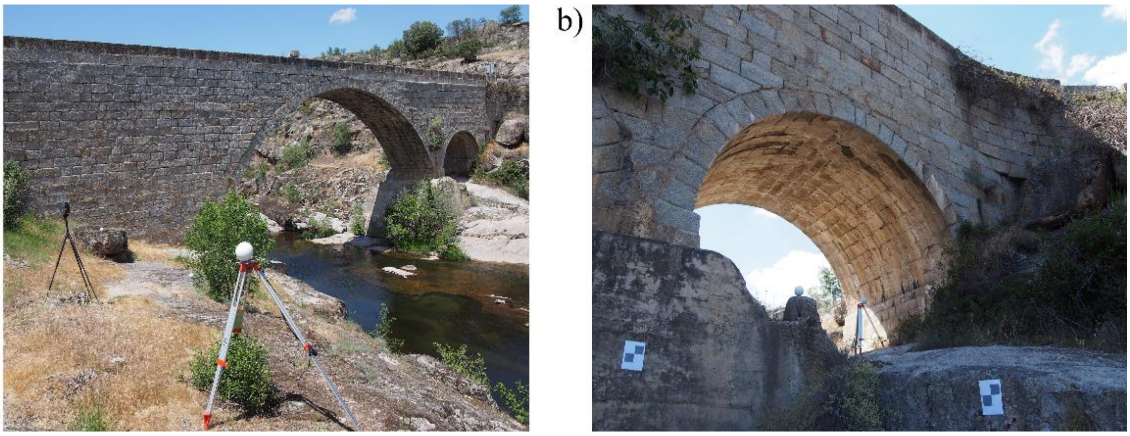

Figure 9: TLS data adquisition: a) TLS Faro Focus 3D 120® and registration spheres used for scanning the bridge; b) registration spheres and planar targets at the lower part of the bridge.

As a consequence, 26 scan stations were needed in order to carry out the 3D digitalization of the whole construction, distributed as follows: (i) a total of 13 scans on the bridge´s deck and (ii) a total of 13 scans under the bridge, resulting from these scans an alignment error of 0.009 ± 0.008 m. Taking into account the goal of the point cloud, the creation of a suitable CAD model for further numerical simulations, it was required the use of additional procedures with the aim of simplifying the large amount of data captured (62,689,274 points). To this end, the procedure proposed by [5] was used. From this process, a more simplified 3D representation of the bridge, with a total of 18,233,172 points (being a 29.08 % of the points of the original point cloud) was obtained (Fig. 10).

Figure 10: 3D representation of the optimized point cloud of the bridge.

3.3 Internal geometrical characterization: Ground Penetrating Radar and the Impact Echo Method

3.3.1 *Ground Penetrating Radar*

The Ground Penetrating Radar (GPR) technique was used with the aim to characterize from the geometrical point of view the distribution of the inner composition of the bridge, as well as the thicknesses of its barrel vaults and its spandrel walls. The equipment used for this purpose was a X3M® GPR system from MALA Geoscience, performing a total of six profiles (Fig. 12): (i) two longitudinal profiles in opposite directions in order to get additional information about the homogeneity and stratification of its infill materials in addition to the thicknesses of the barrel vaults, with a central frequency of 250 MHz and a total time-window of 28 ns and; (ii) four profiles in the vertical directions with the aim of characterizing the thickness of the sprandel walls with a central frequencty of 800 MHz and a total time-window of 104 ns.

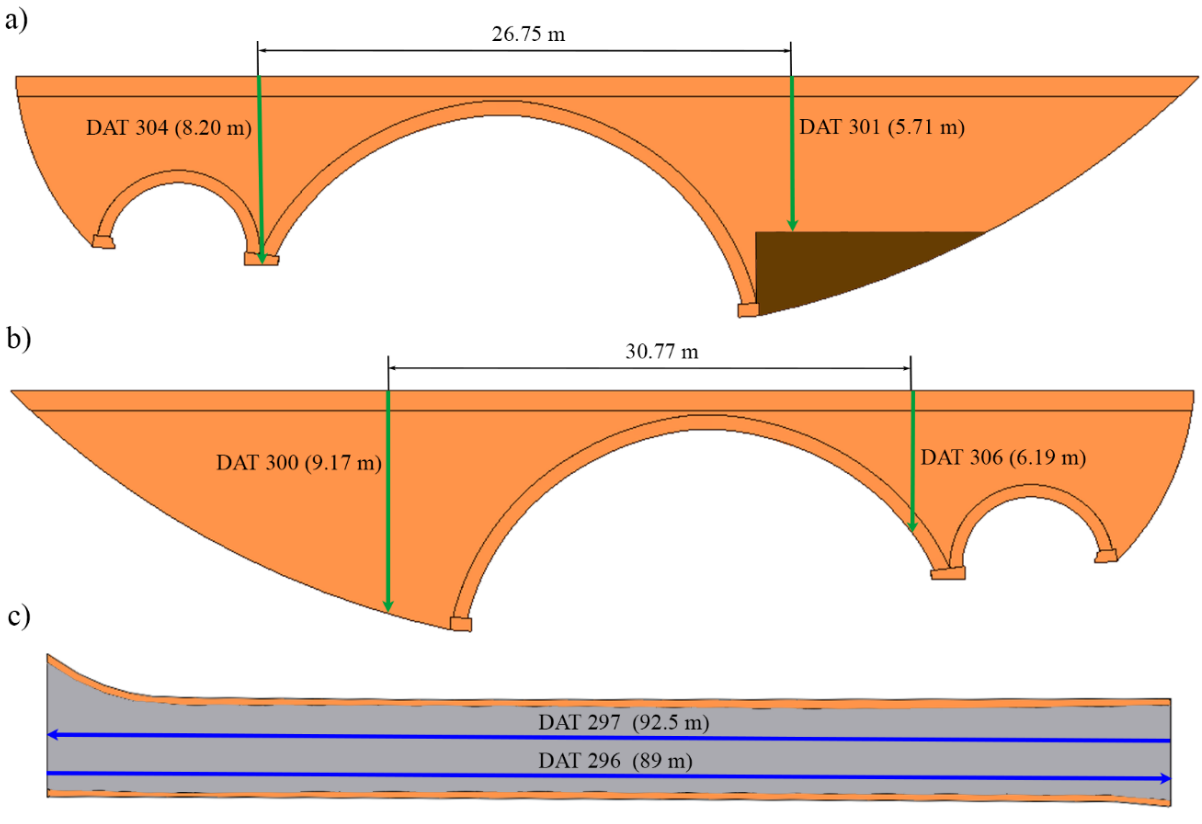

Figure 12: Positions of the GPR tests considered to characterize the inner distribution of the bridge: a) upstream elevation; b) downstream elevation and; c) plant view. In green the vertical profiles and in blue the horizontal profiles.

Each horizontal profile (Fig. 12) (Fig. 13) allowed to identify two different infill layers (Fig. 2) throught the reflection produced between its interfaces until a maximum of 42 ns (2.15 m), whereas the pavement (Fig. 2) was identified by the paving-infill interface at 2 ns (0.20 m). These measurements, were obtained with a pre-calibrated velocity of 0.1

m/ns []. Moreover, these horizontal profiles allowed to estimate the thicknesses of the barrel vaults at an average travel-time distance of 12 ns, corresponding with a thickness value of 0.70 m for the bigger barrel vault, whereas the smaller barrel vault did not appear in the horizontal profiles (Fig. 13a) due to the limited depth of penetration of the system. For this reason, it was assumed a thickness of 0.70 m for the smaller barrel vault according with the drawings of the bridge (Fig. 1a). Furthermore, the thickness measurement of the bigger barrel vault was obtained by the time distance travelled between the reflections of the arch-air interface and the masonry-infill interface, with a pre-calibrated velocity of 0.1 m/ns for granitic ashlar []. It is worth mentioning that the thickness of the asphat and the major barrell vaults were contrasted with the data provided by the last restoration project due to the amount of geometrical uncertainity obtained by the 250 MHz GPR antenna.

On the other hand, the vertical profiles (Fig. 12) (Fig. 13) allowed to identify the thickness of the spandrel walls by means of the reflection produced in the masonry-infill interface due to the dielectric contrast between media and the reflections patterns of the infill. Therefore, with the difference between this reflection and the direct-wave reflection at the surface level (air-masonry interface), the thickness of the spandrel walls was estimated at 10 ns (0.60 m), with a precalibrated velocity of 0.13 m/ns [].

Also it was possible to observe a high amount of reflections in the area of the masonry, suggesting the presence of holes on the interface between the masonry and the infill as well as in the masonry joints, being in accordance with the visual inspection and the mechanical values obtained during the sonic tests (Fig. 3) (Table 2).

PUBLISHED VERSION (DOI): 10.1016/j.ymssp.2019.04.043

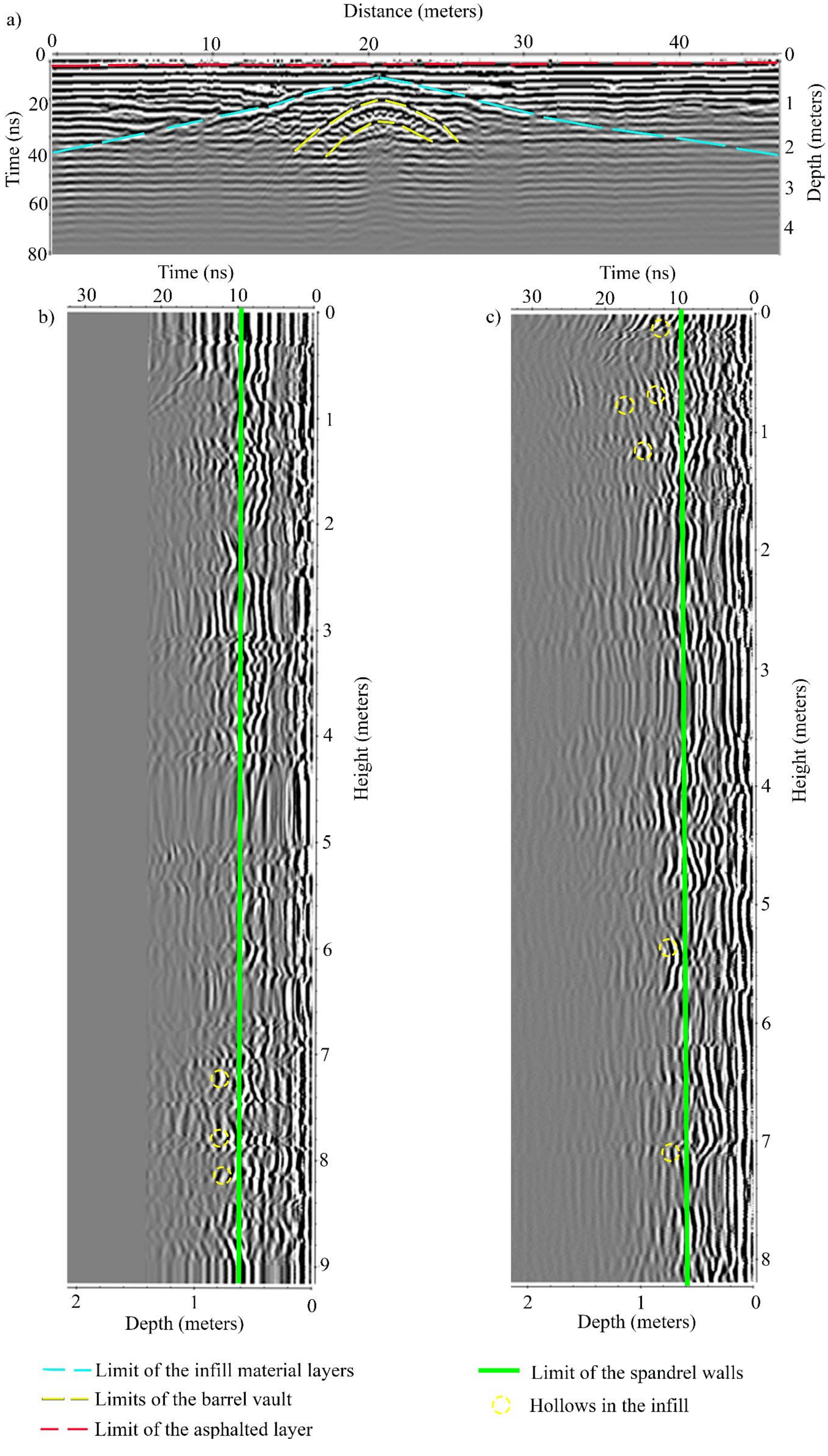

269

Figure 11: Results obtained by the ground penetrating radar: a) asphalted layer, infill material layers and barrel vault thickness; b) and c) thickness of the spandrel walls and hollows in the infill layers.

3.3.2 *Impact Echo Method*

The Impact Echo Method was used with the purpose of ensuring and comparing the thicknesses of the spandrel walls obtained from the vertical profiles by the GPR (Fig. 11b)(Fig. 11c). This test allowed the determination of changes in the inner composition of solids (e.g. cracks into elements made by concrete) by means of the Fourier analysis of the wave generated during the excitation of the material [21]. During these tests, the same instruments than those used for indirect sonic testing were considered. In this case, the instrumental hammer and the transducers were placed in the same position (Fig. 12a), allowing to consider the starting and ending point as the same point. The excitation captured by the transducer was later transformed to the frequency spectrum by means of the Fast Fourier Transfom (FFT) (Fig. 12b). The peaks of this spectrum denotes the presence of inhomogeneities inside the material and thus the interface between the masonry and the infill.

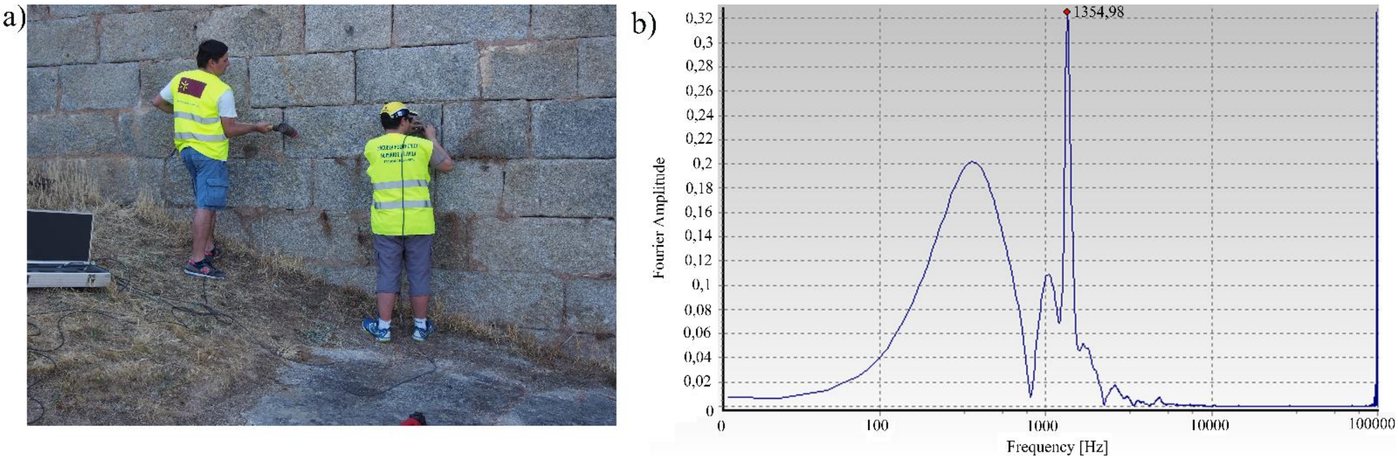

Figure 12: Impact echo tests carried out on the bridge: a) instrumented hammer and accelerometer and; b) identified peak from the frequencies obtained by the Fourier´s spectrum.

According with this, 3 impact echo tests were carried out in different points of the bridge (Fig. 8). With the aim of obtaining reliable results, a total of 10 impacts were carried out on each point. Then, the FFT and the Equation 4 were applied with the aim of obtaining the thickness of the sprandel walls (Table 5). It is worth mentioning, that this equation requires the knowledge of the velocity of the material, using to this end, the velocity (V_p) of the stone obtained during the sonic testing (Table 3).

$$V_P = \ 2df \qquad (4)$$

where V_p is the velocity of the P-wave in m/s of the stone; d is the thickness of the material in m; and f corresponds to the frequency of the peak in Hz.

Table 5: Comparison between the spandrel walls thicknesses obtained by the impact echo tests regarding average spandrel walls thickness obtained by the GPR.

Number of stone	Average velocity of the P-waves (m/s)	Average frequency (Hz)	Thickness (m)	Average thickness (GPR)	Difference (%)
Stone 1	1113.14	915.53	0.61	0.60	1.67
Stone 2	1146.56	791.63	0.72	0.60	20.00
Stone 3	1113.80	1298.83	0.43	0.60	28.33

As a result, an average spandrel wall thickness of 0.59 m was obtained, with a difference of 1.67 % regarding the average spandrel wall thickness obtained by the GPR (0.60 m) (Table 5).

3.4 Dynamical identification: ambient vibration tests (AVT)

Based on the Operational Modal Analysis (OMA) approach, a dynamical identification campaign was carried out in order to identify the dynamic properties of the masonry arch bridge namely: (i) frequencies; (ii) modal displacements and (iii) damping ratios. With the aim of obtaining better results, several numerical evaluations (eigenvalues analysis) were carried out. In this context, the results obtained by the tests and procedures previously shown were considered (CAD model and mechanical properties of the different structural components), as well as different boundary conditions (all degrees of freedom fixed and all degrees of freedom fixed except the Y-axis translation). These previous dynamic simulations allowed to establish the most suitable configuration for the OMA tests (such as its acquisition time and sampling rate) in addition to place the accelerometers in the most proper areas of the bridge.

Taking into account the results obtained from these previous simulations, three setups with an acquisition time of 20 min and a sampling rate of 256 Hz were used. On each setup, a total of 12 uniaxial piezoelectric accelerometers, with a sensitivity of 10 V/g, range of ± 0.5g and 8μg rms broadband resolution, were placed along the bridge´s pavement. From the 12 accelerometers used during the tests, 7 of them were considered as references (fixed positions) in the following directions (Fig. 13): (i) accelerometers (3), (4), (5) and (10) in the Z direction and; (ii) accelerometers (2), (4) and (6) in the Y direction.

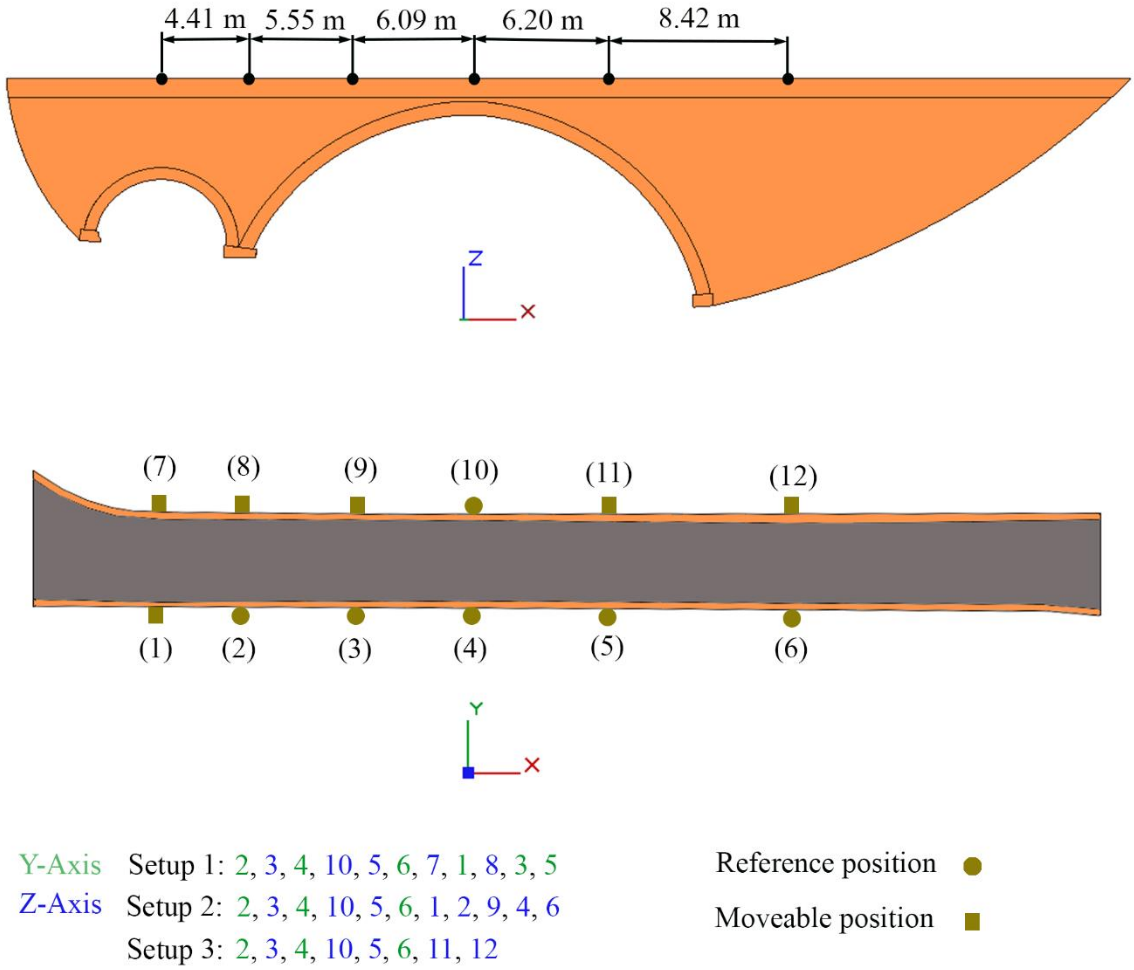

Figure 13: Setups and positions of the accelerometers used during the dynamical identification campaign.

Finally, to obtain the dynamic properties of the bridge, the Stochastic Subspace Identification Principal Component algorithm (SSI-PC), based on raw time series, was used to determine the frequencies, damping ratios and modal shapes [22]. As a result, a total of 5 modes were identified, obtaining frequencies with a range between 5.56 Hz and 18.09 Hz (Table 6) (Fig. 14). The low coefficients of variation (Cov) for the frequencies and damping ratios revealed the quality of the obtained modal properties. Regarding the damping ratio, an average value of 3.48 % was obtained.

Table 6: Natural frequencies and damping ratios obtained from the AVT.

Mode shape	Frequencies (Hz)	CoV (%)	Damping ratios (%)	CoV (%)	Description
1	5.56	0.02	2.53	1.60	1st asymmetrical translational (Y-axis)
2	8.22	<0.01	2.29	2.50	2nd asymmetrical translational (Y-axis) 1st asymmetrical torsional (X-axis)
3	9.31	0.02	4.30	1.83	3rd asymmetrical translational (Y-axis) 1st asymmetrical vertical bending (Z-axis)

4	11.47	0.04	3.63	2.47	2nd asymmetrical vertical bending (Z-axis)
5	18.09	0.03	4.65	2.87	4th asymmetrical translational (Y-axis) 2nd asymmetrical torsional (X-axis)

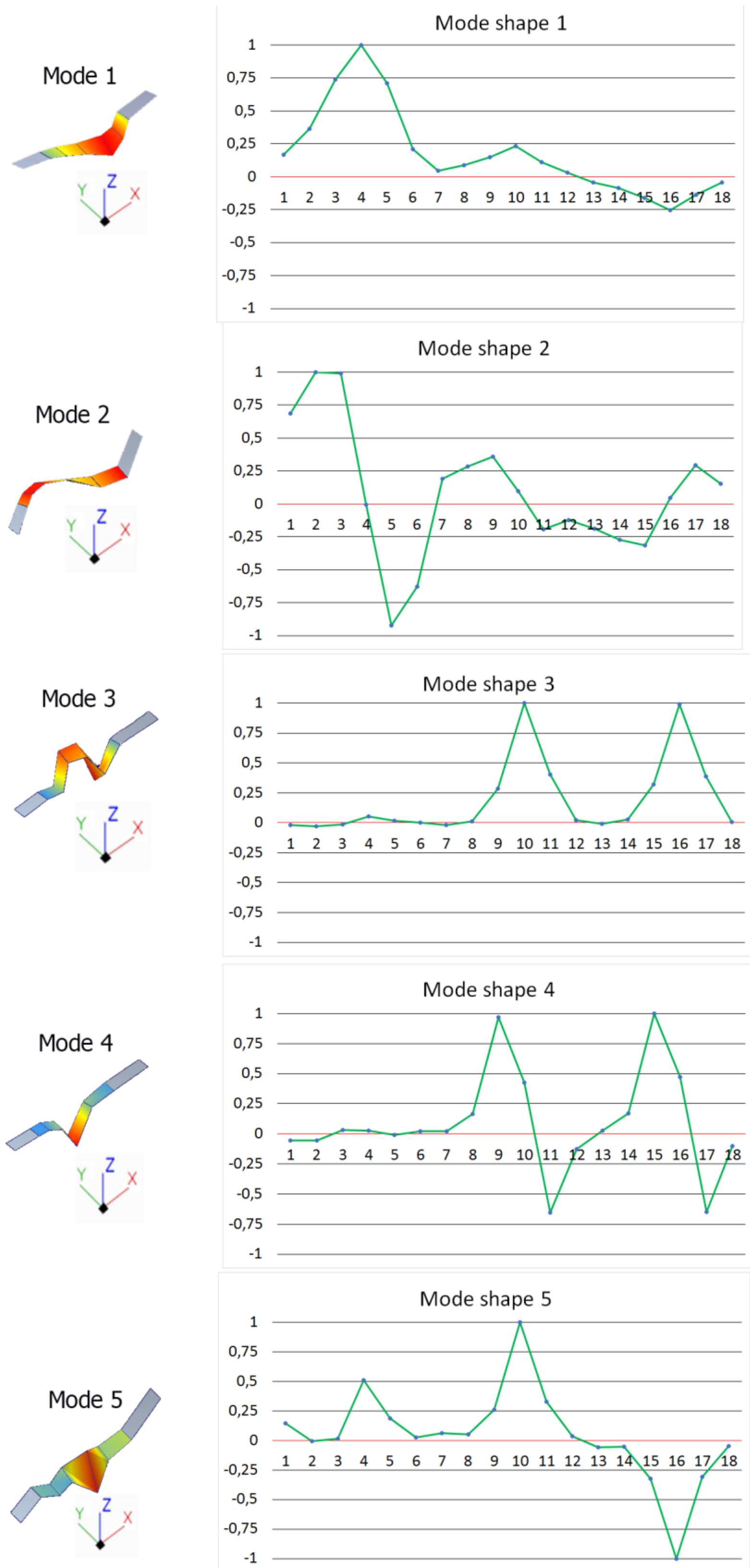

Figure 14: Graphical representation of the vibrational modes obtained by the SSI-PC algorithm. The green line are the experimental modal displacements. The horizontal axis and the vertical axis of the graphs represent the degree of freedoms and the normalized modal displacements, respectively.

4. Numerical model of the current state of the bridge

The robust structural evaluation of masonry arch bridges requires, not only, the development of extensive experimental campaings with the aim of characterizing the structure from different points of view, but also, the accurate desing of numerical models able to reproduce the stuctural behaviour against different casuistic such static or seismic loads. In this sense, the use of the finite element method (FEM) have been placed as one of the most used solutions for the structural evaluation of bridges [1, 5, 13].

4.1 From the point cloud to the numerical model

Taking into consideration all the data provided by the experimental campaign, an as-built CAD model was performed. This CAD model was created with the external envelop coming from the TLS (Fig. 10) and the inner distribution of the different infills and thickness of the masonry from the GPR and the impact-echo tests (Fig. 11) (Section 3.3.2).

This as-built CAD model was carried out by means of the methodology defined by [5]. This methodology comprises the following stages: (i) aligment of the point cloud according with the main axis of the bridge (Fig. 15) and (ii) construction of the CAD model by means of reverse engineering procedures.

For the first stage, a Principal Component Analysis was applied over the whole point cloud through the use of the following equations (Eq. 5)(Eq. 6). This evaluation allowed to obtain the maximum dispersion direction (third eigen-vector) which corresponds with the longitudinal axis of the bridge. Then, a rotation along the *z* axis was carried out with the aim of aligning the *x* axis of the point cloud with the longitudinal axis of the bridge (Fig. 15).

$$V_i = \frac{1}{n-1}\sum_{m=1}^{n}(X_{im} - \bar{X}_i)^2 \tag{5}$$

$$C_{ij} = \frac{1}{n-1}\sum_{m=1}^{n}(X_{im} - \bar{X}_i)^2(X_{jm} - \bar{X}_j)^2 \tag{6}$$

where V_i and C_{ij} are the variance and the covariance of each variable *i* and *j* ; *n* is the number of points of the data matrix from the point cloud, $\sum_{m=1}^{n}$ is the sum over all *n* points; X_{im} is the value of each variable *i*; X_{jm} is the value of each variable *j*; $\bar{X}_i$ is the mean of the variable *i* and; $\bar{X}_j$ is the mean of the variable *j*.

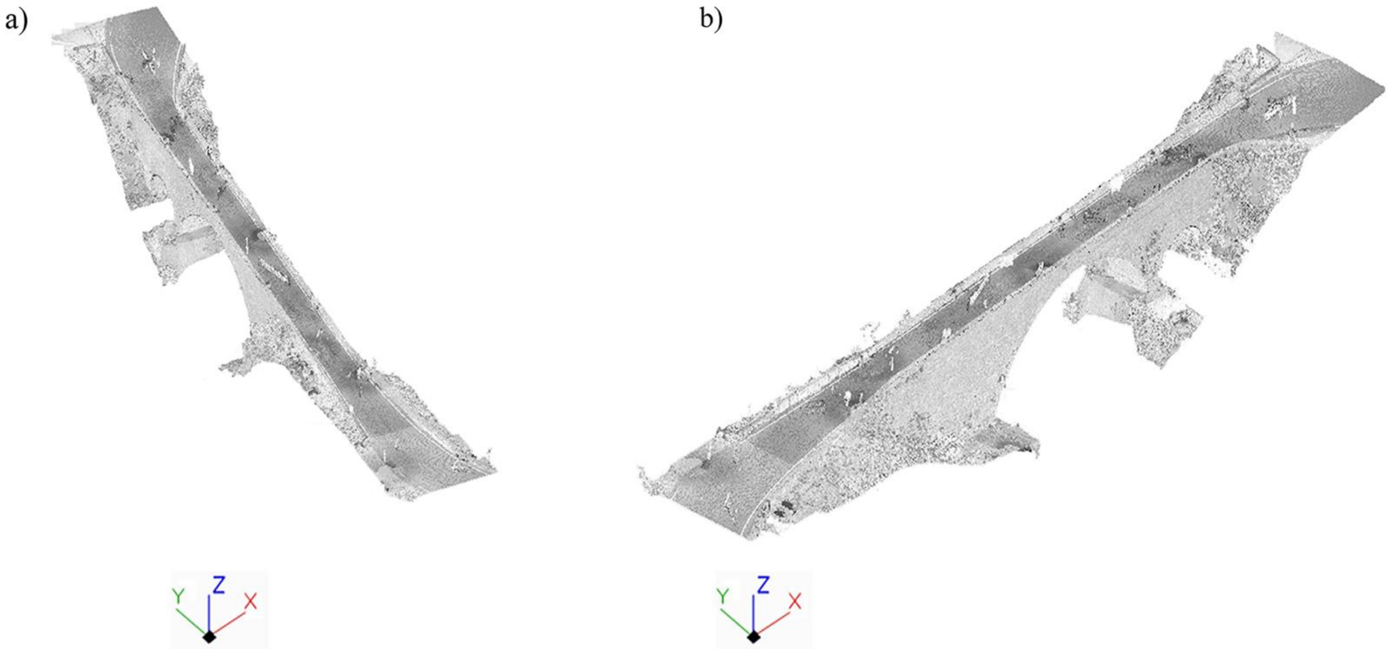

Figure 15: Results applying the methodology proposed by [5] : a) original point cloud; b) rotated point cloud.

Concerning the second step, the multistep geometrical modelling method proposed by [23] was used. This methodology is based on the following stages: (i) Delaunay triangulation of the aligned point cloud; (ii) hole filling based on radial basis functions [24]; (iii) topological noise removal by means of a local re-triangulation [25]; (iv) segmentation of the different structural components and (v) adjustment of segmented elements into basic primitives based on linear and non-linear (b-splines) extrusions. As a result, a mesh composed by a total of 9,567,843 triangles was transformed into a suitable and accurate CAD model of the bridge for the subsequent numerical simulations (Fig. 16).

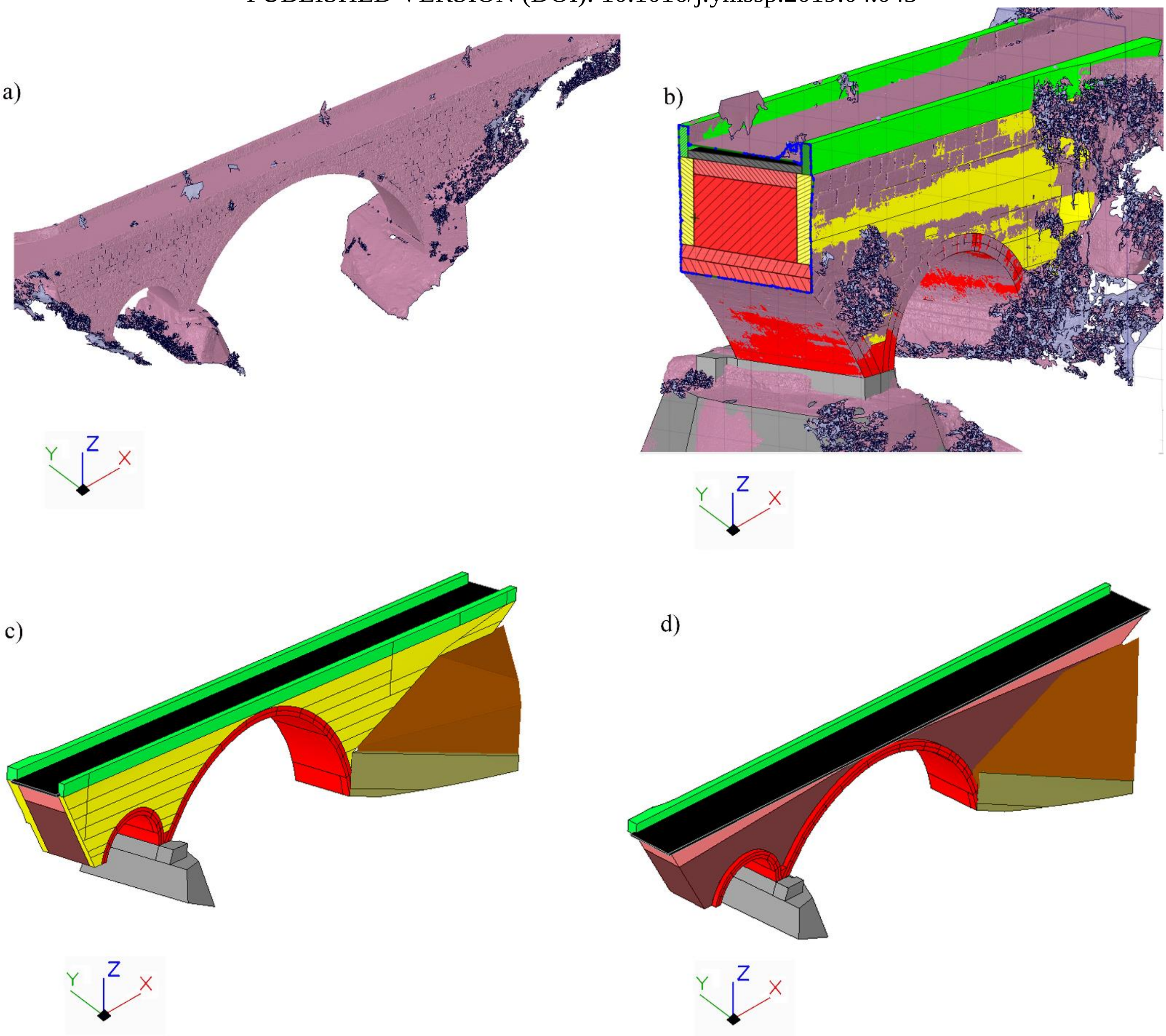

Figure 16: As-built CAD model obtained: a) isometric view of the mesh obtained from the rotated point cloud; b) detail of the accuracy between the CAD model and the mesh c) isometric view of the as-built CAD model and d) isometric view of the infill material layers.

Finally, the FEM method was applied in the CAD model in order to perform further numerical simulations, using to this end the software TNO Diana® [26]. As a result, a mesh composed by a total of 128,884 elements was obtained (Fig. 17): (i) 127,089 solid elements for the structural components and; (ii) 1,795 interface elements to simulate the interaction of the bridge with the soil. This mesh was built assuming the following criterions: (i) maximum size of the element 1m; (ii) minimum size of 0.3 m in order to better represent the geometry of the as-built CAD model and (iii) a minimum of 2 elements in the tickness direction of the barrel vaults with the purpose to identifiy possible non-linearities in further non-linear assessments.

However, although the numerical model is detailed from the point of view of each structural element in the best possible way, some simplifications were assumed taking account the feasibility of the model development and the computational cost reduction in subsequent numerical simulations. Thus, the thickness of the spandrel walls and barrel vaults was assumed constant over the whole height and width, respectively. Furthermore, the wing wall and the reinforced concrete pier were not included in the final model since can be considered as perfect fixed structures (Fig. 17) (Fig. 18).

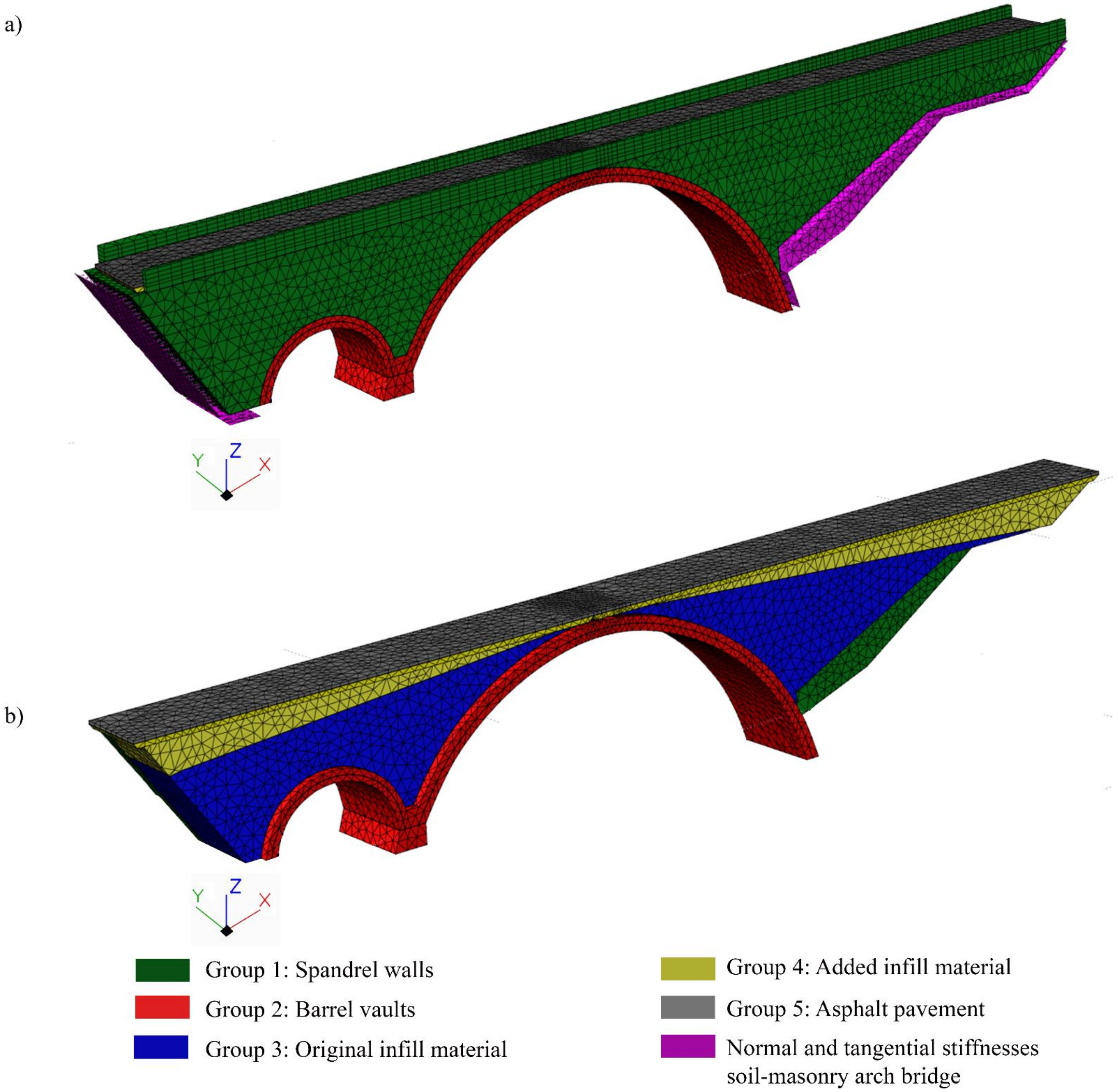

Figure 17: Mesh model used for the numerical simulations: a) bridge´s envelop and b) inner distribution of the bridge.

4.2 *First results from the numerical model of the Arco Bridge*

Considering the mean values of the mechanical parameters obtained during the experimental campaign (Table 1) (Table 2) (Table 7) and assuming a boundary conditions in agreement with the bridge´s surrounding medium (all degrees of freedom fixed with infinite normal and shear stiffnesses in all interface elements), an initial assessment was performed (Fig. 17). With the aim of evaluating the accuracy of the numerical model, two qualitiy indexes were considered: (i) relative error between numerical and experimental frequencies and (ii) the analysis of the discrepancies between modal displacements through the use of the Modal Assurance Criterion (MAC) [27]. The results obtained from the evaluation of the different quality indexes revealed a rigid structure (high relative error between frequencies, especially in the mode 1), as well as moderate discrepancies in the modes 2 and 3 (transversal modes) with respect to the modal displacements (Table 8) (Fig. 18).

Table 7: Average values of the Young´s modulus and densities calculated from the values obtained during the sonic tests (Groups 1 and 2) and MASW tests (Groups 3 and 4). With respect to the asphalt pavement (Group 5), the average values proposed by Von Quintos [28] were assumed.

Group	Elastic modulus (GPa)	Density (kg/m3)
Group 1	1.78	2250
Group 2	3.29	2250
Group 3	1.73	1909
Group 4	0.41	1819
Group 5	2.41	2237

Table 8: MAC values and numerical frequencies obtained from the initial model compared with the experimental frequencies obtained from the AVT.

Vibration modes	*fexp* (Hz)	*fnum* (Hz)	Relative error (%)	MAC
1	5.56	5.31	4.45	0.95
2	8.22	8.11	1.37	0.80
3	9.31	9.48	1.81	0.82
4	11.47	11.36	0.95	0.96
5	18.09	18.02	0.40	0.87

a) b)

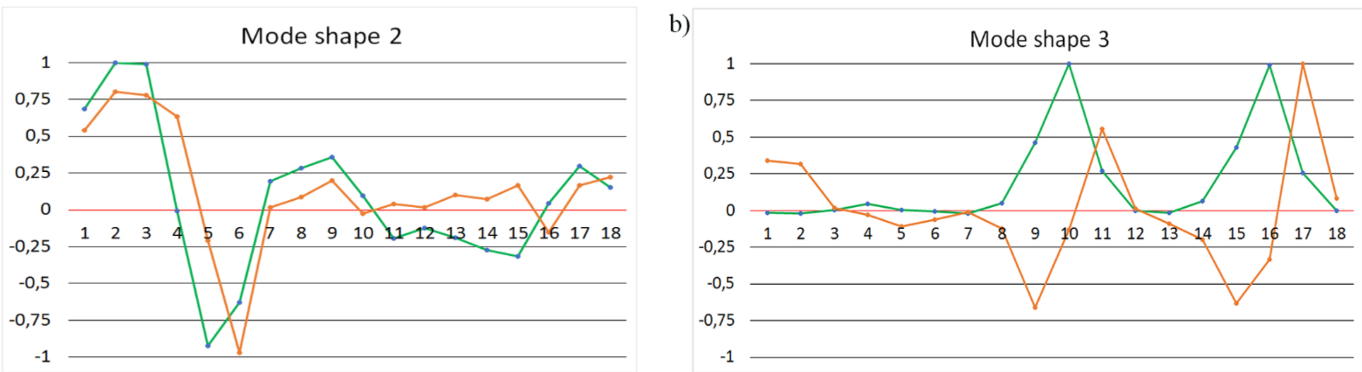

Figure 18: Comparison between experimental and numerical modal displacements of the mode shape 2 and the mode shape 3. In green the experimental modal displacements and in orange the numerical ones. The vertical axis of the graphs represent the normalized modal displacements and the horizontal axis the degree of freedoms.

According with the previous results (Table 8) (Fig. 18) it was possible to observe some discrepancies in the first frequency and lower MAC values in the 2nd and 3rd eigenmodes, suggesting the necesity of using an updating method to enhance the results.

With the aim of evaluating more in depth the origin of the discrepancies in the 2nd and 3rd eigenmodes, the coordinate modal assurance criterion (COMAC) [27] was used. As a result, it was possible to observe a concentration of discrepancies in the following degrees of freedom (Fig. 19): (i) the first degree of freedom in the Y- axis direction; and (ii) the fourth and tenth degrees of freedom in the Z-axis direction. These discrepancies correspond with the mid-span of the bigger barrel vault as well as an iteration soil-bridge (see Section 3.3).

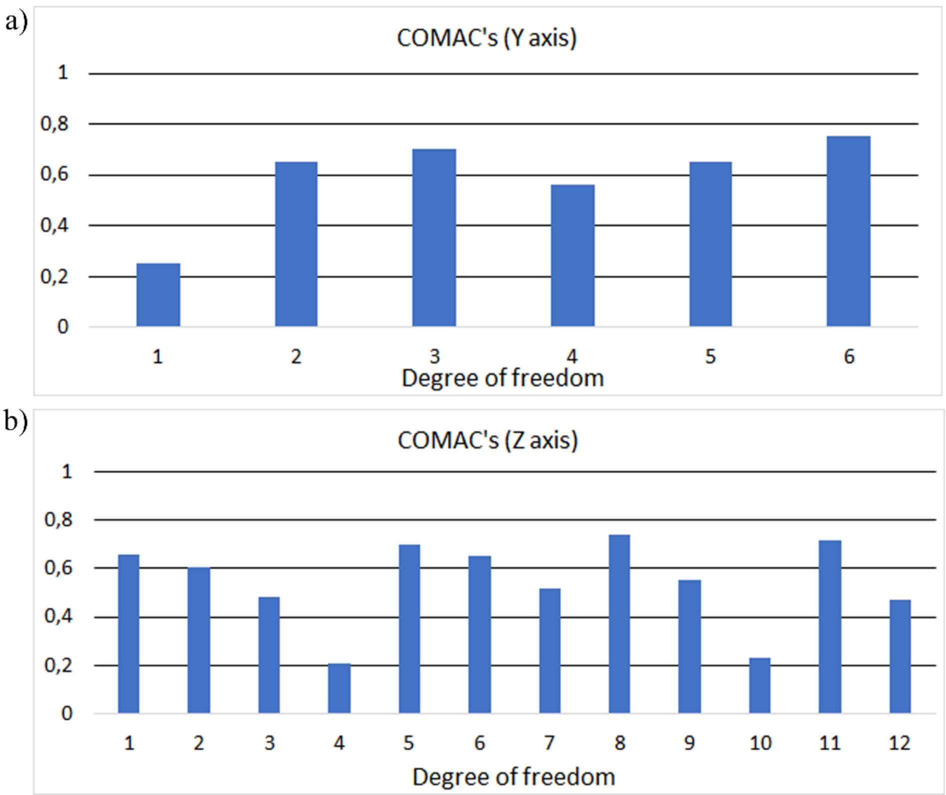

Figure 19: COMAC values obtained from the first simulation: a) COMAC values in Y axis and b) COMAC values in Z axis.

4.3 Numerical model updating strategy

Considering the results obtained in the previous section (Table 8) (Fig. 18) (Fig. 19), an uptating procedure was carried out. During this procedure, the following stages were considered: (i) global sensitivity analysis and (ii) minimization of the cost function.

4.3.1 *A global sensitivity analysis based on the combination of Polynomial Chaos Expansion and the Sobol's indexes.*

Global sensitivity analysis aims at determining how the variability of the model response (frequencies and modal displacements) is affected by the value of the inputs paremeters (variables of the model). A common and robust technique is based on the descomposition of the response variance as a sum of contributions that can be associated to each input: the so-called Sobol´s indexes [14]. Commonly, these indexes are evaluated through the use of Monte Carlo simulations, requiring thousand of simulations to obtain reliable results and being this strategy non-viable in those cases on which the computational costs of the numerical model are high [15].

Taking this into account, a reliable alternative pass through the use of the so-called subrrogate models. These models are compact and scalable analitic models that approximate the input output response of a complex system, in this case an advanced numerical simulation approximations of the original computational model, requiring only a limited number of runs to obtain accurate results (7).

$$\mathrm{x} \epsilon D_x \subset R^d \rightarrow y = \tilde{f}(x) \tag{7}$$

where x are the input parameters; D_x the space of these parameters, y the output of the subrrogate and $\tilde{f}(x)$ the subrrogate model.

Inside the wide variety of metamodels that can be used nowadays, from Krigging metamodels to radial basis functions [29], the polynomial chaos expansion (PCE) is one of the most used, allowing the evaluation of sensitivity indices and their interation [29]. In this method, it is assumend that the numerical simulation can be represented as a finite variance model *M(X)* whose inputs x are a random vector of independent constrained variables $X \in \mathbb{R}^M$. Each one of these inputs are described as a joint probability density function (PDF) *fx*. Considering this, the computational model can be represented by means of the following equation (Eq. 13).

$$\mathrm{Y} \approx \tilde{f}(\mathrm{X}) = \sum_{\alpha \in N^M} y_\alpha \, \psi_\alpha(X) \tag{8}$$

where Y is the computational model, $\psi_\alpha(X)$ is the multivariate orthonormal polynomial with respect to *fx(x)*, $\alpha \in \mathbb{N}^M$ is a multi-index that locates the components of the multivariate polynomials ψ_α and the $y_\alpha \in \mathbb{R}$ are the respective coefficients (coordinates) and; M is the number of input variables.

From a practical point of view, the sum of Equation 13 requires to be truncated to a finite sum of the truncated polynomial chaos expansion (Eq. 14) [30]:

$$Y \approx \tilde{f}^{PCE}(X) = \sum_{\alpha \in A} y_\alpha \, \psi_\alpha(X) \tag{14}$$

where $M^{PCE}(X)$ is the polynomial chaos expansion surrogate model; $\alpha = \{\alpha_1 \ldots \alpha_d\}$ are the indexes of the polynomial chaos expansion; $A \in \mathbb{N}^M$ is the set of indexes α corresponding to the truncation scheme; $X = (X_1, X_2, \ldots, X_d)$ is the multivariate vector of the input parameters considered and; ψ_α is the multivariate polynomial.

Moreover, the multivariate polynomials (ψ_α) that include the PCE basis are obtained through the tensorization of suitable univariate polynomials. It is worth mentioning, that each univariate polynomial was constructed by employung the classical families of polynomial proposed by []. It was used Legendre polynomials for those inputs with a uniform PDFs and Hermite polynomials for inputs with Gaussian PDFs. Then, the multivariate polynomials $(\psi_\alpha)(X)$ are assembled as the tensor product of their univariate polynomials. For the calculation of the coefficients, it was employed a non-intrusively strategy based on the least-square minimization proposed by [31].

On the other hand, the set of multi-indices *A* of the Equation 14 is obtained by means of a suitable truncation scheme, which consists in the selection of the multivariate polynomials up to a total degree p^t, i.e. $\{\psi_\alpha, \alpha \in \mathbb{N}^M : \sum_{i=1}^{M} \alpha_i \leq p^t\}$. Therefore, the corresponding number of terms in the truncated series is defined as (Eq. 15):

$$cardA = \binom{M + p^t}{p^t} = \frac{(M + p^t)!}{M!\,p^t!} \tag{15}$$

where *M* are the input variables of the polynomial; and *p* the degree of the polynomials.

It is important to highlighting, that the truncated polynomial chaos expansion shown in Eq. 13 can be descomposed into summands of increasing order, similar to the definition of the Sobol indices. Then, for any non-empty set $u \subset \{1, \ldots, M\}$ and any finite truncation set $A \subset \mathbb{N}^M$, it can be defined that $A_u = \{\alpha \in A : k \in u \Leftrightarrow \alpha_k \neq 0, k = 1, \ldots M\}$. This means that A_u encompasses all multi-indices within the truncation set *A* which have non-zero components $\alpha_k \neq 0$ if and only if $k \in u$. Moreover, the sum of the associated terms from the PCE creates a function which depends only on the input variables x_u. Due to the orthonormality of the PCE, the variance of the truncated model can be expresed as (Eq. 16) (Eq. 17):

$$Var[Y_A] = \sum_{\substack{\alpha \in A \\ \alpha \neq 0}} \hat{y}_\alpha^2 \tag{16}$$

$$Var[f_v(X_v)] = \sum_{\substack{\alpha \in A \\ \alpha \neq 0}} \hat{y}_\alpha^2 \tag{17}$$

where Y_A is the truncated model; and $f_v\,(x_v)$ is the expresion of each summand for the polynomical chaos expansion.

Considering the expresions previously shown, the Sobol´s indices can be expresed as (Eq. 18)(Eq.19):

$$\hat{S}_i = \frac{\sum_{\alpha \in A} \hat{y}_\alpha^2}{\sum_{\alpha \in A, \alpha \neq 0} \hat{y}_\alpha^2} \text{ where } A_i = \{\alpha \in A : \alpha_i > 0, \alpha_{j \neq i} = 0\} \tag{18}$$

$$\hat{S}_i^t = \frac{\sum_{\alpha \in A^t} \hat{y}_\alpha^2}{\sum_{\alpha \in A\ \ , \alpha \neq 0} \hat{y}_\alpha^2} \text{ where } A_i^T = \{\alpha \in A : \alpha_i > 0\} \tag{19}$$

where $\widehat{S}_i$ and $\widehat{S}_i^t$ are the first-order and total Sobol´s indices of the output variable i; $\hat{y}$ and α are the coefficients and indexes of the polynomial chaos expansion respectively and A the subset of input variables. The first-order Sobol´s indices $\hat{S}\ i$ representes the effect of each input variable alone in the model´s variance. Meanwhile, the total Sobol´s indices represents the full effect of each input variable (alone and in combination with other input variables) in the output model´s variance.

According with the approach previously defined, a total of 100 metamodels were built with the aim of evaluating the first five frequencies as its associated modal displacements (90 per each mode). Furthermore, the validation of these metamodels was carried out by means of the Leave One Out error (LOO error) (Eq. 20) [32, 33]. This metric of error shows a good compromise between fair error estimation and affordable computational cost.

$$LOO\ error = \frac{1}{N} \sum_{i=1}^{N} \left(\frac{Y\left(X^{(i)}\right) - \tilde{f}^{PCE}\left(X^{(i)}\right)}{1 - h_i} \right)^2 \tag{20}$$

where $Y\left(X^{(i)}\right)$ is the computational model ; $\tilde{f}^{PCE}\left(X^{(i)}\right)$ is the subrrogate model obtained form a specific DoE and; h_i is the i-th diagonal term of matrix $A(A^TA)^{-1}A^T$; and A the experimental matrix.

Once the most sensitivity variables have been obtained, the next step was the minimization of the discrepancies between the numerical and the experimental data. To this end, the following cost function was considered (Eq. 9).

$$\pi = \frac{1}{2}\left[W_f \sum_{i=1}^{n} \left(\frac{f_{i,num}^2 - f_{i,exp}^2}{f_{i,exp}^2} \right)^2 + W_{\emptyset} \sum_{j=1}^{m} (1 - MAC)^2 \right] \tag{9}$$

where π is the cost function to be minimized, composed of the residuals of the relative error between the numerical $f_{i,num}$ and experimental frequencies $f_{i,exp}$ as well as the MAC values. The terms *n* and *m* of this cost function represent the number of frequencies and mode shapes assumed in the calibration of the numerical model respectively, whereas W_f is the frequency weight and $W_\emptyset$ is the MAC weight. With the aim to balance the contributions of the frequencies and MAC of the residuals of the objetive function, the values for the W_f and the $W_\emptyset$ were assumed as three and one, respectively.

Taking into consideration the possible non-linear relation between the residuals of the cost function and the input variables, the minimization problem was formulated as a non-linear least-squares problem on which was used the iterative Gauss-Newton method to minimize the cost function (LS). This method was complemented by the Trust Region Reflective algorithm as proposes [13]. Within this iterative minimization problem, the gradient and the Hessian of the objective function were calculated as follow (Eq. 10) (Eq. 11).

$$\nabla\pi(\theta) = J(\theta)^T r(\theta) \tag{10}$$

$$\nabla^2(\theta) = J(\theta)^T J(\theta) + \sum_{i=1}^{k} r_i(\theta)\nabla^2 r_i(\theta) \cong J(\theta)^T J(\theta) \tag{11}$$

where *r* is the *k* -dimensional vector of frequency and mode shape residuals, θ represents the vector of input variables, and *J* indicates the Jacobian or sensitivity matrix, containing the first partial derivates of the residuals with respect to the input variables. These derivates were calculated by means of the finite difference strategy.

Taking into consideration that the optimization strategy previously shown is a local minimization method, and with the aim of finding the global minimum of the cost function, a multistart approach was carried out. This approach runs several optimization problems, starting each from a different initial point. These initial points were created with the Latin Hypercube Sampling method (LHS) [34].

4.4 **Calibrated model**

Considering the workflow proposed in the previous section, an updating process of the numerical model previously defined was carried out (Fig. 17). To this end, an initial set of variables were considered namely: (i) four Young Modulus (*E1* to *E4*) corresponding to the groups of masonry and infill materials; (ii) two densities (*d1* and *d2*) corresponding to the masonry of the spandrel walls and barrel vaults and; (iii) two normal stiffnesses (*Kn1* and *Kn2*) and four shear stiffnesses in the X-direction and Y-direction ($Kt1_x$, $Kt1_y$ and $Kt2_x$, $Kt2_y$) at the extremes of the bridge in order to simulate the possible interaction between the bridge and the soil. It is worth mentioning that the inputs *d3,d4,E5,d5* were not considered during the sensitivity analysis with the aim of reducing the complexity of the subrrogate model. On the one hand, *d3* and *d4* were not considered due to their low variance in comparison with the rest of variables. On the other hand, *d5* and *E5* were not included since it is expected that their contribution will be low in comparison with the variables previously cited.

Taking into consideration this set of variables, and under the premises defined in section 4.3.1, different PCE-metamodels were built with the aim of evaluating the Sobol's indexes of each output variable (5 frequencies and 90 modal displacements). During these evaluations, different sample sizes were considered with the aim of generating the optimum metamodel of each output (best relation between the number of evaluation and the accuracy of the model). The samples of the DoE were extracted in a sequential way, using to this end the sequential Latin Hypercube Sampling (LHS) methodolgoy as propose Liu et al. During this stage it was used as constriction the upper and lower bounds of the variables obtained during the experimental campaign (Table 9).

Table 9: Upper and lower bounds considered during the updating stage. The upper and lower bounds of the support´s stiffnesses, the Young Modulus (*E5*) and the density (*d5*) of the asphalt pavement were extrated from Chen & Bathurst [35] and Von Quintus [28], respectively.

Parameter	**Upper bounds**	**Lower bounds**
E1 (GPa)	2.56	1.00
E2 (Gpa)	4.00	2.57
E3 (Gpa)	3.18	0.56
E4 (Gpa)	0.78	0.33
d1 (kg/m^3)	2500	2000
d2 (kg/m^3)	2500	2000
$Kn1$(N/m^3)	1.00×10^8	1.00×10^6
$Kt1_x$(N/m^3)	1.00×10^8	1.00×10^6
$Kt1_y$(N/m^3)	1.00×10^8	1.00×10^6
$Kn2$(N/m^3)	1.00×10^8	1.00×10^6
$Kt2_x$(N/m^3)	1.00×10^8	1.00×10^6
$Kt2_y$(N/m^3)	1.00×10^8	1.00×10^6

According with the Table 10, it was possible to conclude that the optimum design of experiment (DoE) of the metamodel is 500, showing an average LOO error of 2.19×10^{-3}. This DoE corresponds with 50 times the number of input variables used as input to represent the response of the numerical model. Taking into consideration this, the PCE metamodels built with 500 samples were considered for the calculation of the Sobol's indexes (Fig. 20).

Table 10: LOO error in frequencies output variables and average LOO error in modal displacements output variables for different sizes of the DoE. Dm_i is the average value of the modal displacements for the mode *i*.

	Number of samples obtained with the LHS					
Output variable	**100**	**200**	**300**	**400**	**500**	**600**
f1	5.27×10^{2}	1.80×10^{-2}	7.48×10^{-3}	1.06×10^{-5}	3.17×10^{-6}	1.14×10^{-6}
f2	3.06×10^{2}	2.16×10^{-2}	1.38×10^{-2}	1.73×10^{-5}	6.76×10^{-6}	8.21×10^{-6}
f3	1.90×10^{-1}	1.02×10^{0}	1.01×10^{0}	1.01×10^{-1}	8.90×10^{-5}	8.12×10^{-5}
f4	3.93×10^{3}	2.37×10^{-2}	2.25×10^{-2}	3.32×10^{-4}	1.37×10^{-5}	1.43×10^{-5}
f5	1.69×10^{-2}	4.26×10^{-1}	4.12×10^{-1}	3.71×10^{-3}	2.57×10^{-5}	1.36×10^{-5}
dm1	2.18×10^{3}	1.65×10^{-1}	1.09×10^{-1}	9.08×10^{-4}	5.78×10^{-5}	4.17×10^{-5}
dm2	3.83×10^{2}	4.94×10^{-1}	4.99×10^{-1}	4.53×10^{-4}	3.30×10^{-4}	3.71×10^{-4}
dm3	3.08×10^{3}	4.71×10^{-1}	4.59×10^{-1}	3.85×10^{-1}	5.04×10^{-3}	4.76×10^{-3}
dm4	6.10×10^{5}	8.63×10^{-1}	8.09×10^{-1}	7.76×10^{-3}	7.84×10^{-3}	7.57×10^{-3}
dm5	3.77×10^{4}	9.96×10^{-1}	8.75×10^{-1}	9.34×10^{-3}	8.46×10^{-3}	8.60×10^{-3}

Moreovert, to corroborate this optimum DoE, the First-order Sobol´s indices between the DoE with different sizes were compared in order to see the variation between subsequen DoE. As a result from this comparison, the minimum average variations of the first order Sobol´s indices were obtained between the DoE with 500 samples and the DoE with 600 samples (Table 11).

Table 11: Average variation of the Sobol´s indices between different sizes of DoE.

Parameter	**100-200 samples**	**200-300 samples**	**300-400 samples**	**400-500 samples**	**500-600 samples**
E1	4.03	2.32	1.53	0.25	0.01
d1	0.00	0.00	0.00	0.00	0.00
E2	2.17	1.23	0.75	0.12	0.02
d2	0.00	0.00	0.00	0.00	0.00
E3	3.56	2.95	0.52	0.31	0.01
E4	4.52	2.13	1.15	0.43	0.02
Kn1	5.34	3.51	1.23	0.51	0.01
$Kt1_x$	4.83	3.49	1.36	0.47	0.02
$Kt1_y$	3.32	2.67	1.05	0.17	0.02
Kn2	3.26	2.81	0.93	0.10	0.01
$Kt2_x$	3.76	2.52	0.81	0.18	0.02
$Kt2_y$	3.52	2.79	1.07	0.15	0.01

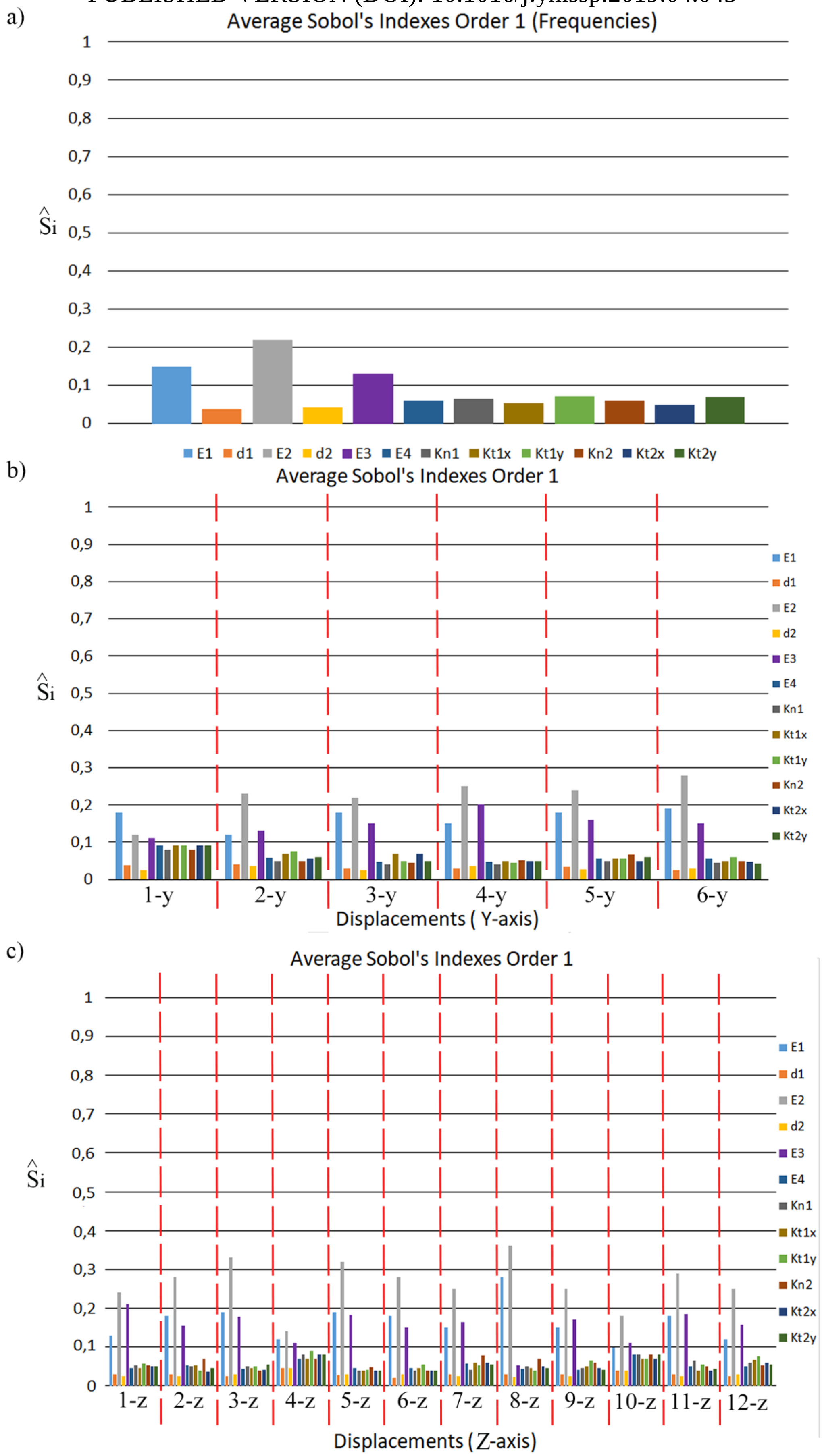
a)
Average Sobol's Indexes Order 1 (Frequencies)
Ŝi
1
0,9
0,8
0,7
0,6
0,5
0,4
0,3
0,2
0,1
0
E1 d1 E2 d2 E3 E4 Kn1 Kt1x Kt1y Kn2 Kt2x Kt2y
b)
Average Sobol's Indexes Order 1
Ŝi
1-y
2-y
3-y
4-y
5-y
6-y
Displacements (Y-axis)
c)
Average Sobol's Indexes Order 1
Ŝi
1-z
2-z
3-z
4-z
5-z
6-z
7-z
8-z
9-z
10-z
11-z
12-z
Displacements (Z-axis)

Figure 20: Average first order Sobol's indexes ($\hat{S}_i$) obtained during the global sensitivity analysis of the numerical model: a) Average first order Sobol's indexes of the first five eigenfrequencies; b) Average first order Sobol's indexes of the Y-axis modal displacements and c) Average first order Sobol's indexes of the Z-axis modal displacements.

From the sensitivity analysis it was possible to conclude that the variance of the output model is strongly influenced by the variace of each input alone since the First-order Sobol´s indices are similar to the Total Sobol´s indices. On the one hand, the frequencies are strongly influenced by the inputs *E1, E2* and *E3*, showing average First-order Sobol indices of 0.19, 0.29 and 0.16 respectively. That means that the 19%, 29% and 16% of the output variance is caused by the variance of these inputs. Regarding the modal displacements, it was possible to observe that these inpunts, *E1,E2* and *E3* are the most sensitive variables with average First-order Sobol´s indice of 0.18,0.26 and 0.17 respectively. For the rest of the inputs it wa possible to observe that the different variables that define the interaction bridge-soil ahas a similar impact in the output variance. The densities (*d1* and *d2)* are the inputs with less impact in the output variance, specially in the frequencies of the model.

Higher average first order Sobol's indexes were obtained in the frequencies (Fig. 20a) for the Young Modulus *E1*, *E2*, and *E3* corresponding to the Group 1 (spandrel walls), Group 2 (barrel vaults) and Group 3 (original infill material) respectively, being initially the most sensitive parameters. With the aim to identify more parameters with high sensitivity, the degrees of freedom (DOF) with the lower COMAC values from the initial model were associated with the corresponding DOF of the average first order Sobol's indexes of the displacements (the first DOF in the Y-axis direction and the fourth and tenth DOF in the Z-axis direction) (Fig. 19) (Fig. 20b) (Fig. 20c), allowing to identify the Young Modulus *E4* corresponding to the Group 4 (added infill material) and all the stiffnesses that represent the interaction between the bridge and the soil ($Kn1$, $Kt1_x$, $Kt1_y$, $Kn2$, $Kt2_x$ *and* $Kt2_y$) as the most sensitive parameters together with *E1, E2* and *E3.* Therefore, a total of 10 parameters were considered to carry out the subsequent updating process. It is worth mentioning that during this stage it was used the average values of the inputs *d1,d2,d3,d4,d5* and *E5* to calibrate the model (Table 1)(Table 7).

Finally, a minimization of the cost function was carried out by means of the optimization strategy defined in Section 4.3.2 (LHS+LS). In this case, a total of 20 samples coming from the LHS method were considered as starting points for the minimization problem (Table 11). As a result of these 20 minimizations, it was possible to find a minimum on which the numerical model shown an average relative error in frequencies of 1.21% and an average MAC value of 0.93 (Table 11). It is worth mentioning, that the updated values of the masonry structural elements and the infill materials of the numerical model (Table 12) are approximated with respect to the average values obtained from the experimental campaign (Table 1) (Table 2), corroborating the robustness of the calibrated numerical model and the experimental tests carried out on the bridge (MASW and sonic tests).

Table 12: Values of each one of the 20 samples coming from the LHS method obtained for the sensitive parameters. These values were used as starting points during the calibration of the numerical model of the bridge.

Sample	***E1*** **(GPa)**	***E2*** **(GPa)**	***E3*** **(GPa)**	***E4*** **(GPa)**	***Kn1*** **(N/m³)**	***Kt1ₓ*** **(N/m³)**	***Kt1ᵧ*** **(N/m³)**	***Kn2*** **(N/m³)**	***Kt2ₓ*** **(N/m³)**	***Kt2ᵧ*** **(N/m³)**
1	2.03	3.32	1.23	0.42	5.27×10^7	6.54×10^7	6.54×10^7	3.28×10^7	2.26×10^7	2.26×10^7
2	2.54	2.24	1.81	0.32	4.31×10^7	2.31×10^7	2.31×10^7	5.21×10^7	1.45×10^7	1.45×10^7
3	1.47	3.93	1.98	0.39	2.13×10^7	1.37×10^7	1.37×10^7	4.31×10^7	3.51×10^7	3.51×10^7
4	2.45	3.17	1.65	0.47	3.71×10^7	5.76×10^7	5.76×10^7	2.56×10^7	2.29×10^7	2.29×10^7
5	1.81	2.61	1.49	0.34	1.82×10^7	2.67×10^7	2.67×10^7	1.38×10^7	1.15×10^7	1.15×10^7
6	1.07	3.41	1.70	0.53	6.31×10^7	5.83×10^7	5.83×10^7	3.17×10^7	2.62×10^7	2.62×10^7
7	1.30	3.16	1.33	0.36	7.11×10^7	4.41×10^7	4.41×10^7	5.21×10^7	3.45×10^7	3.45×10^7
8	1.67	3.57	1.03	0.56	4.38×10^7	3.16×10^7	3.16×10^7	2.68×10^7	1.93×10^7	1.93×10^7
9	2.39	3.26	1.85	0.37	2.94×10^7	2.77×10^7	2.77×10^7	1.81×10^7	1.35×10^7	1.35×10^7
10	2.17	3.78	1.63	0.53	3.55×10^7	2.91×10^7	2.91×10^7	2.64×10^7	2.12×10^7	2.12×10^7
11	2.09	3.69	1.20	0.34	1.71×10^7	1.28×10^7	1.28×10^7	2.96×10^7	1.73×10^7	1.73×10^7
12	1.65	3.89	1.07	0.38	2.94×10^7	2.33×10^7	2.33×10^7	3.52×10^7	2.51×10^7	2.51×10^7
13	1.29	2.82	1.15	0.31	4.21×10^7	3.27×10^7	3.27×10^7	5.13×10^7	3.47×10^7	3.47×10^7
14	1.80	3.11	1.61	0.45	5.16×10^7	4.71×10^7	4.71×10^7	4.67×10^7	2.95×10^7	2.95×10^7
15	1.41	2.72	1.23	0.51	2.73×10^7	1.56×10^7	1.56×10^7	3.21×10^7	2.67×10^7	2.67×10^7
16	1.97	3.86	1.74	0.44	3.51×10^7	2.73×10^7	2.73×10^7	4.15×10^7	2.38×10^7	2.38×10^7
17	1.58	3.25	1.29	0.41	2.19×10^7	1.91×10^7	1.91×10^7	3.67×10^7	2.14×10^7	2.14×10^7
18	1.38	3.09	1.78	0.47	1.87×10^7	1.76×10^7	1.76×10^7	2.44×10^7	1.65×10^7	1.65×10^7
19	1.51	3.13	1.81	0.49	3.61×10^7	2.73×10^7	2.73×10^7	4.10×10^7	2.42×10^7	2.42×10^7
20	1.31	3.77	1.54	0.56	2.54×10^7	2.21×10^7	2.21×10^7	3.59×10^7	2.67×10^7	2.67×10^7

Table 11: Discrepancies obtained from the second calibration in terms of relative error in frequencies (*f*) and MAC values. In brackets, values obtained from the initial model.

Vibration modes	***fexp*** **(Hz)**	***fnum*** **(Hz)**	Relative error (%)	MAC
1	5.56	5.45 (5.31)	2.03 (4.48)	0.96 (0.95)
2	8.22	8.27 (8.11)	0.72 (1.37)	0.92 (0.80)
3	9.31	9.23 (9.48)	0.87 (1.81)	0.90 (0.82)
4	11.47	11.53 (11.36)	0.56 (0.95)	0.97 (0.96)
5	18.09	17.76 (18.02)	1.86 (0.41)	0.91 (0.87)

Table 12: Comparison between the initial numerical model and the updated numerical model.

Parameter	Upper bounds	Lower bounds	Initial numerical model	Updated numerical model
E1 (GPa)	2.56	1.00	1.79	1.91
E2 (GPa)	4.00	2.57	3.28	3.62

E3 (GPa)	3.18	0.56	1.73	0.97
E4 (GPa)	0.78	0.33	0.41	0.51
$Kn1$(N/m^3)	1.00×10^8	1.00×10^6	-	1.88×10^7
$Kt1_x$(N/m^3)	1.00×10^8	1.00×10^6	-	1.83×10^7
$Kt1_y$(N/m^3)	1.00×10^8	1.00×10^6	-	1.83×10^7
$Kn2$(N/m^3)	1.00×10^8	1.00×10^6	-	3.34×10^7
$Kt2_x$(N/m^3)	1.00×10^8	1.00×10^6	-	1.01×10^7
$Kt2_y$(N/m^3)	1.00×10^8	1.00×10^6	-	1.01×10^7

Finally, Figure 21 reveals a comparison between the experimental and numerical mode shapes from a graphic point of view (Fig. 14). Assessing all results (Table 12) (Fig. 14), can be considered that the results obtained from the updated numerical model presents a better correlation regarding the experimental results obtained from the AVT, especially in the discrepancies observed in the 2nd and 3rd vibrational modes, improving their MAC values from an initial value of 0.80 and 0.82 for the 2nd and 3rd mode to 0.92 and 0.90 , respectively. Reaffirming the importance of the influence of the boundary conditions in the dynamic behaviour of the bridge.

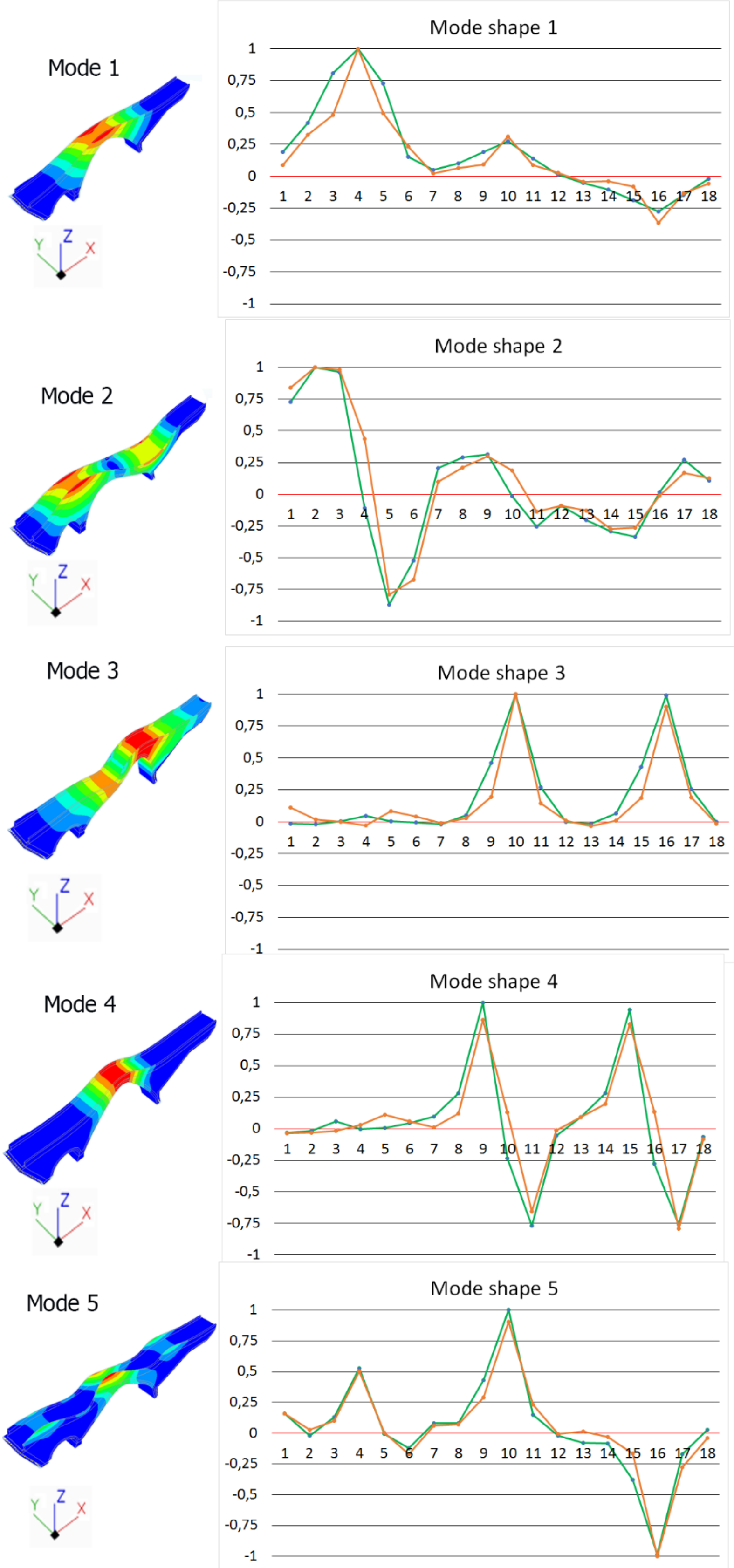

Figure 21: Graphical comparison between experimental (green) and numerical (orange) modal shapes obtained from the updated numerical model. The horizontal axis of the graphs represent the degree of freedoms and the vertical axis the normalized modal displacements.

5. Conclusions

In this paper a robust multidisciplinary approach was proposed with the aim of obtaining accurate numerical simulations of masonry arch bridges by means of the finite element method. This methodology, fully based on non-destructive methods, enhances the current multidisciplinary methods for the structural assessment of masonry bridges at different levels.

At material and geometrical level, the proposed methodogy considers, in comparison with the traditional multidisciplinary methodology, the use of several wave-based approaches, such as the multichannel analysis of surface waves or the sonic testing with the aim of characterizing accurately the different materials presented in the bridge. It is worth mentioning the values obtained for the "Original infill layer" which can be justified by the presence of some intrusions of natural soil within the space delimited by the sprandell walls. The combination of the methods within the terrestrial laser scanner, the ground penetrating radar as well as reverse engineering procedures, allows to create as-built CAD models of masonry bridges. This methodology is able to reproduce possible non-parametric shapes presented on this types of structures in contrast with other methodologies on which the CAD model is created thorugh the extraction of section coming from the point cloud. Additionally, the proposed methodology was able to characterize the mechanical and physical properties of the infill not requiring, as other multidisciplinary approaches, the use of values coming from the literature or the application of invasive methods based on the extraction of samples.

Concerning the numerical field, the finite element model derived from the proposed methodology shows a good correlation with respect to the ground truth (ambient vibration tests). This model shows a error in frequencies of about 1.80% and an average MAC value of 0.88, demonstrating the robustness of the multidisciplinary approach. This correlation was enhanced thanks to the use of an updating method based on the combination of a Polynomial Chaos Expansion metamodel and the Sobol's indexes for the sensitivity analysis and a non-linear least squares optimization approach. It is worth mentioning, the great efficiency and accuracy of the Polinomial Chaos Expansion metamodel for the sensitivity analysis, requiring a low number of interations in comparison with the classical MonteCarlo approach.In our case, and considering that the input variables used to built the subrrogate model were 10, it was needed a total of 500 points for the DoE (about 50 times the number of variables). Additionally, the ability of analyzing the Sobol indices from the Polinomial Chaos Expasion allow to evaluate, in a robust way, the influence of each input in the output variance, instead of using basic sensitivity analysis or correlation methods (e.g. Spearman matrix).

This updating approach allowed the creation of a numerical model with a relative error in frequencies of 1.21% and an average MAC value of 0.93. During this stage, and taking into account the nature of the optimization algorithm used, which is prone to being trapped into local optima, a total of 20 optimization runs were carried with the aim of explore the search space and obtaining a possible global minimum. The starting point of each run was obtained by means of the LHS method. On each run, it was spent 4,836 seconds to rearch the minimum. Result of this, it was spent a total of 109,320 seconds during the updating stage: i) 12,600 seconds for the senstitivity analysis (PCE + Sobol) and; ii) 96720 seconds for the optimization (Non-Linear Squares + Gauss-Newton) in a processor Intel® XEON E3-1240 v3 at 3.4 Ghz and 8Gb RAM DDRII.

Finally, with regards to future works, these could contemplate to carry out them on several fields. On the one hand, several numerical analysis will be carry out with the aim of evaluating the current structural performance against static (traffic loads) and dynamic (such as earthquakes) situations, as well as the use of adaptative smapling strategies, such as those proposed by Brut et al. based on the LOLA-VORONOI algorithm. On the other hand, further research will be focused on a depth evaluation of the MASW method with the aim of characterizing the non-linear properties of the infill, namely: (i) cohesion and (ii) friction angle; as well as the use of additional methods such as the electric resistivity tomography in order to obtain and in-depth evaluation of the bridge infill topology. Additionally, and taking into consideration the uncertainity associated with the data obtained by the 250 MHz GPR antenna, several impact-echo tests will be carried out on the barrel vaults and on the asphalt with the aim of corroborating the thicknesses provided by the GPR and the historical drawings. Added to this, several radiometric classifications, based on the acquired data from the TLS system, will be performed in order to complete the damage evaluation of the construction, by means of the use of the pixel-based classification methods.

Acknowledgments

This work was financed by ERDF funds through the V Sudoe Interreg program within the framework of the HeritageCARE project, Ref. SOE1/P5/P0258. This research has been also partially supported by Patrimonio 5.0 funded by Junta of Catilla y León, Ref. SA075P17**.** Second author would like to thank the University of Salamanca for the program for human resources “Programa II: Contratos Postdoctorales”.

References

[1] B. Conde, L.F. Ramos, D.V. Oliveira, B. Riveiro, M. Solla, Structural assessment of masonry arch bridges by combination of non-destructive testing techniques and three-dimensional numerical modelling: Application to Vilanova bridge, Engineering Structures, 148 (2017) 621-638 https://doi.org/10.1016/j.engstruct.2017.07.011.

[2] B. Riveiro, J. Caamaño, P. Arias, E. Sanz, Photogrammetric 3D modelling and mechanical analysis of masonry arches: An approach based on a discontinuous model of voussoirs, Automation in Construction, 20 (2011) 380-388 https://doi.org/10.1016/j.autcon.2010.11.008.

[3] D. Ribeiro, R. Calçada, R. Delgado, M. Brehm, V. Zabel, Finite element model updating of a bowstring-arch railway bridge based on experimental modal parameters, Engineering Structures, 40 (2012) 413-435 https://doi.org/10.1016/j.engstruct.2012.03.013.

[4] M. Stavroulaki, B. Riveiro, G. Drosopoulos, M. Solla, P. Koutsianitis, G.E. Stavroulakis, Modelling and strength evaluation of masonry bridges using terrestrial photogrammetry and finite elements, Advances in Engineering Software, 101 (2016) 136-148 https://doi.org/10.1016/j.advengsoft.2015.12.007.

[5] Á. Bautista-De Castro, L.J. Sánchez-Aparicio, L.F. Ramos, J. Sena-Cruz, D. González-Aguilera, Integrating geomatic approaches, Operational Modal Analysis, advanced numerical and updating methods to evaluate the current safety conditions of the historical Bôco Bridge, Construction and Building Materials, 158 (2018) 961-984 https://doi.org/10.1016/j.conbuildmat.2017.10.084.

[6] L.F. Miranda, J. Rio, J.M. Guedes, A. Costa, Sonic Impact Method–A new technique for characterization of stone masonry walls, Construction and Building Materials, 36 (2012) 27-35 https://doi.org/10.1016/j.conbuildmat.2012.04.018.

[7] S. Russo, Integrated assessment of monumental structures through ambient vibrations and ND tests: the case of Rialto Bridge, Journal of Cultural Heritage, 19 (2016) 402-414 https://doi.org/10.1016/j.culher.2016.01.008.

[8] A.S. Gago, J. Alfaiate, A. Lamas, The effect of the infill in arched structures: Analytical and numerical modelling, Engineering Structures, 33 (2011) 1450-1458 https://doi.org/10.1016/j.engstruct.2010.12.037.

[9] B. Conde, L. Díaz-Vilariño, S. Lagüela, P. Arias, Structural analysis of Monforte de Lemos masonry arch bridge considering the influence of the geometry of the arches and fill material on the collapse load estimation, Construction and Building Materials, 120 (2016) 630-642 https://doi.org/10.1016/j.conbuildmat.2016.05.107.

[10] B. Conde, G. Drosopoulos, G. Stavroulakis, B. Riveiro, M. Stavroulaki, Inverse analysis of masonry arch bridges for damaged condition investigation: Application on Kakodiki bridge, Engineering Structures, 127 (2016) 388-401 https://doi.org/10.1016/j.engstruct.2016.08.060.

[11] V. Compan, P. Pachón, M. Cámara, Ambient vibration testing and dynamic identification of a historical building. Basilica of the Fourteen Holy Helpers (Germany), Procedia Engineering, 199 (2017) 3392-3397 https://doi.org/10.1016/j.proeng.2017.09.572.

[12] L.J. Sánchez-Aparicio, B. Riveiro, D. Gonzalez-Aguilera, L.F. Ramos, The combination of geomatic approaches and operational modal analysis to improve calibration of finite element models: A case of study in Saint Torcato Church (Guimarães, Portugal), Construction and Building Materials, 70 (2014) 118-129 https://doi.org/10.1016/j.conbuildmat.2014.07.106.

[13] L.J. Sánchez-Aparicio, L.F. Ramos, J. Sena-Cruz, J.O. Barros, B. Riveiro, Experimental and numerical approaches for structural assessment in new footbridge designs (SFRSCC–GFPR hybrid structure), Composite Structures, 134 (2015) 95-105 https://doi.org/10.1016/j.compstruct.2015.07.041.

[14] I.M. Sobol, Sensitivity estimates for nonlinear mathematical models, Mathematical modelling and computational experiments, 1 (1993) 407-414.

[15] B. Sudret, Global sensitivity analysis using polynomial chaos expansions, Reliability Engineering & System Safety, 93 (2008) 964-979 https://doi.org/10.1016/j.ress.2007.04.002.

[16] E.R. Almeida, Puentes históricos de la provincia de Ávila, Institución Gran Duque de Alba, 2015.

[17] C.B. Park, R.D. Miller, J. Xia, Multichannel analysis of surface waves, Geophysics, 64 (1999) 800-808 https://doi.org/10.1190/1.1444590.

[18] C.S. Blázquez, A.F. Martín, P.C. García, D. González-Aguilera, Thermal conductivity characterization of three geological formations by the implementation of geophysical methods, Geothermics, 72 (2018) 101-111 https://doi.org/10.1016/j.geothermics.2017.11.003.

[19] L. Miranda, L. Cantini, J. Guedes, A. Costa, Assessment of mechanical properties of full-scale masonry panels through sonic methods. Comparison with mechanical destructive tests, Structural Control and Health Monitoring, 23 (2016) 503-516 https://doi.org/10.1002/stc.1783.
[20] H. Yoon, H. Song, K. Park, A phase-shift laser scanner based on a time-counting method for high linearity performance, Review of Scientific Instruments, 82 (2011) 075108 https://doi.org/10.1063/1.3600456.
[21] N.J. Carino, The impact-echo method: an overview, Structures 2001: A Structural Engineering Odyssey, 2001, pp. 1-18 https://doi.org/10.1061/40558(2001)15.
[22] H. Herlufsen, P. Andersen, S. Gade, N. Møller, Identification techniques for operational modal analysis–an overview and practical experiences, Proceedings of the 1st International Operational Modal Analysis Conference, Copenhagen, 2005.
[23] M. Herrero-Huerta, D. González-Aguilera, P. Rodriguez-Gonzalvez, D. Hernández-López, Vineyard yield estimation by automatic 3D bunch modelling in field conditions, Computers and electronics in agriculture, 110 (2015) 17-26 https://doi.org/10.1016/j.compag.2014.10.003.
[24] D. Branch, L.C. Dang, N. Hall, W. Ketchum, M. Melakayil, J. Parrent, M. Troxel, D. Casebeer, D.J. Jeffery, E. Baron, Comparative direct analysis of type Ia supernova spectra. II. Maximum light, Publications of the Astronomical Society of the Pacific, 118 (2006) 560.
[25] I. Guskov, Z.J. Wood, Topological noise removal, 2001 Graphics Interface Proceedings: Ottawa, Canada, (2001) 19.
[26] T. Diana, DIANA finite element analysis, The Netherlands, (2005).
[27] R.J. Allemang, The modal assurance criterion–twenty years of use and abuse, Sound and vibration, 37 (2003) 14-23.
[28] H.L. Von Quintus, Asphalt-aggregate mixture analysis system, AAMAS, Transportation Research Board, 1991.
[29] M. Asher, B. Croke, A. Jakeman, L. Peeters, A review of surrogate models and their application to groundwater modeling, Water Resources Research, 51 (2015) 5957-5973 https://doi.org/10.1002/2015WR016967.
[30] R. Ghanem, P. Spanos, Stochastic Finite Elements: A Spectral Approach, Revisited ed Dover Publications, INC, New York, (2003).
[31] G. Blatman, B. Sudret, Adaptive sparse polynomial chaos expansion based on least angle regression, Journal of Computational Physics, 230 (2011) 2345-2367 https://doi.org/10.1016/j.jcp.2010.12.021.
[32] M. Stone, Cross-validatory choice and assessment of statistical predictions, Journal of the royal statistical society. Series B (Methodological), (1974) 111-147.
[33] S. Geisser, The predictive sample reuse method with applications, Journal of the American statistical Association, 70 (1975) 320-328.
[34] M.D. McKay, R.J. Beckman, W.J. Conover, Comparison of three methods for selecting values of input variables in the analysis of output from a computer code, Technometrics, 21 (1979) 239-245 https://doi.org/10.1080/00401706.1979.10489755 .
[35] J. Chen, R. Bathurst, Investigation of interface toe sliding of reinforced soil block face walls using FLAC, Proceedings of Continuum and Distinct Element Numerical Modeling in Geomechanics, Shanghi, China, Itasca International, (2013).